Mon. Not. R. Astron. Soc. **000**, 1–21 (2001) Printed 3 June 2005 (MN LATEX style file v1.4)

Newtonian hydrodynamics of the coalescence of black holes with neutron stars – IV: Irrotational binaries with a soft equation of state

William H. Lee
Instituto de Astronomía, Universidad Nacional Autónoma de México, Apdo. Postal 70–264, Cd. Universitaria, 04510 México D.F.

3 June 2005

ABSTRACT

We present the results of three–dimensional hydrodynamical simulations of the final stages of inspiral in a black hole–neutron star binary, when the separation is comparable to the stellar radius. We use a Newtonian Smooth Particle Hydrodynamics (SPH) code to model the evolution of the system, and take the neutron star to be a polytrope with a soft (adiabatic index $\Gamma = 2$ and $\Gamma = 5/3$) equation of state and the black hole to be a Newtonian point mass. The only non–Newtonian effect we include is a gravitational radiation back reaction force, computed in the quadrupole approximation for point masses. We use irrotational binaries as initial conditions for our dynamical simulations, which are begun when the system is on the verge of initiating mass transfer and followed for approximately 23 ms. For all the cases studied we find that the star is disrupted on a dynamical time–scale, and forms a massive ($M_{disc} \approx 0.2\ M_{\odot}$) accretion torus around the spinning (Kerr) black hole. The rotation axis is clear of baryons (less than $10^{-5} M_{\odot}$ within 10°) to an extent that would not preclude the formation of a relativistic fireball capable of powering a cosmological gamma ray burst. Some mass (the specific amount is sensitive to the stiffness of the equation of state) may be dynamically ejected from the system during the coalescence and could undergo r–process nucleosynthesis. We calculate the waveforms, luminosities and energy spectra of the gravitational radiation signal and show how they reflect the global outcome of the coalescence process.

Key words: binaries: close — gamma rays: bursts — gravitational waves — hydrodynamics — stars: neutron

1 INTRODUCTION AND MOTIVATION

In binary systems, the emission of gravitational waves and accompanying loss of angular momentum will lead to a decrease in the orbital separation, and coalescence will occur if the decay time is small enough (less than the Hubble time). For binaries made of neutron stars, PSR 1913+16 being the most famous example, this consequence of general relativity has been observed indirectly (Hulse & Taylor 1975) (see also Wolszczan (1991) for the case of PSR 1534+12), and the change in orbital period matches the theoretical predicion to very high accuracy (Taylor et al. 1992; Stairs et al. 1998). Given their present–day orbital periods (on the order of 10 hours), these systems will eventually merge. The final stages of the coalescence present an opportunity to study the equation of state at very high densities (the system is in effect a giant accelerator), and will undoubtedly produce a strong electromagnetic and gravitational wave signal containing some of this information. No black hole–neutron star binary systems are known yet, but population synthesis studies (Lattimer & Schramm 1976; Narayan, Piran & Shemi 1991; Tutukov & Yungelson 1993; Lipunov, Postnov & Prokhorov 1997; Bethe & Brown 1998; Portegies Zwart & Yungelson 1998; Belczyński & Bulik 1999; Kalogera et al. 2001; Kalogera & Belczyński 2001) over the past 25 years lead one to believe that their rate is comparable to that of double neutron star binaries, and is on the order of $10^{-6} - 10^{-5}$ per year per galaxy.

Solving this problem completely clearly requires detailed hydrodynamic modeling in three dimensions, radiation transport, a realistic equation of state, and general relativity. As such, it must be approached in stages, with successive approximations depending on the aspect of the general problem one wishes, and is able, to solve.

Compact binaries are expected to be sources of gravitational radiation observable by detectors such as LIGO (Abramovici et al. 1992) and VIRGO (Bradaschia et al.

1990) as the inspiral occurs. The signal can be approximated as that of point–masses and calculated accurately using post–Newtonian expansions when the separation is large, compared with the stellar radius (Kidder, Will & Wiseman 1992; Cutler et al. 1994; Blanchet et al. 1995). When the distance between the stars becomes comparable to their radii, hydrodynamical modeling becomes essential. The theoretical study of the tidal disruption of a neutron star by a black hole was addressed many years ago (Wheeler 1971; Lattimer & Schramm 1974; Lattimer & Schramm 1976), and numerical hydrodynamical studies of binary neutron star coalescence were begun somewhat more recently, initially by Oohara & Nakamura (1989; 1990; 1992) and Nakamura & Oohara (1989; 1991). The work of Chandrasekhar (1969) on incompressible ellipsoids was generalized to the compressible case in the Newtonian regime by Lai, Rasio & Shapiro (1993b, hereafter LRSb), using a polytropic equation of state, who showed that tidal effects alone could produce a de–stabilization of the orbit in certain situations (Lai, Rasio & Shapiro 1993a). Rasio & Shapiro (1992; 1994; 1995, hereafter RS92, RS94, RS95 respectively) then performed a series of dynamical simulations to study the coalescence of two neutron stars, using Smooth Particle Hydrodynamics (SPH), while Zhuge, Centrella & McMillan (1994; 1996) focused on the gravitational waves spectrum. Both of these groups used a polytropic equation of state throughout their analysis. The thermodynamical details of the process were studied by Davies et al. (1994), Ruffert, Janka & Schäfer (1996), Ruffert et al. (1997) and Rosswog et al. (1999; 2000), by using the equation of state of Lattimer & Swesty (1991). This work was all done using a Newtonian or modified Newtonian approach (by including gravitational radiation reaction in different ways in the calculations), and we note that the thermodynamic details are of little importance for the emission of gravitational waves, since it is concernced primarily with the motion of bulk matter at high densities. More recently, there have been advances in making post–Newtonian calculations of initial conditions (Lombardi, Rasio & Shapiro 1997) and mergers (Faber & Rasio 2000; Faber, Rasio & Manor 2000; Ayal et al. 2001), and also in including general relativity (Wilson, Mathews & Marronetti 1996; Baumgarte et al. 1997; Oohara & Nakamura 1999; Shibata 1999; Shibata & Uryū 2000; Uryū & Eriguchi 2000; Usui, Uryū & Eriguchi 2000; Gourgoulhon et al. 2001).

The gamma ray burts (GRBs) are now believed to be at cosmological distances (Meegan et al. 1992), after the discovery of optical afterglows (Mészáros & Rees 1997a) in the last few years that have established their redshifts (Metzger et al. 1997; Djorgovski et al. 1998; Kulkarni et al. 1998; Kulkarni et al. 1999). Reviews have been given by Fishman & Meegan (1995) and van Paradijs, Kouveliotou & Wijers (2000). Observations have shown that (i) there is a bimodality in burst durations (Kouveliotou et al. 1995), with classes of short ($t_{burst} \simeq 0.5$ s) and long ($t_{burst} \simeq 40$ s) bursts; (ii) the energy release if one assumes isotropy is on the order of $10^{51} - 10^{53}$ erg; (iii) many bursts show variability on very short (ms) time–scales; (iv) at least some bursts are beamed, implying a lower energy release than isotropic emission would lead one to believe (see e.g. Harrison et al. (1999); Stanek et al. (1999); Frail et al. (2001)). The preferred model for GRBs involves the expansion of a relativistic fireball (Rees & Mészáros 1992; Mészáros & Rees 1993)

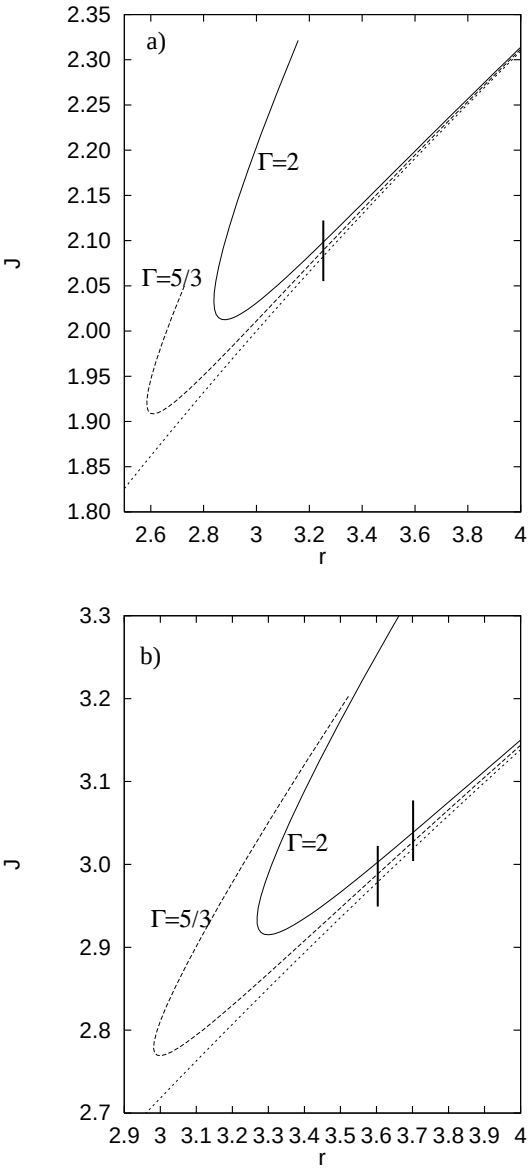

which would produce the gamma rays through relativistic shocks and subsequent synchrotron radiation. The fireball would presumably originate from a central engine capable of accomodating the observational requirements mentioned above. A variety of progenitors involving compact objects have been suggested, see e.g. Fryer, Woosley & Hartmann (1999a). Many of them invoke an accretion torus around a black hole, originating from a double neutron star coalescence (Goodman 1986; Paczyński 1986; Eichler et al. 1989; Narayan, Paczyński & Piran 1992), where the central object would presumably collapse to a black hole, the merger of a neutron star, white dwarf or Helium core with a black hole (Paczyński 1991; Fryer et al. 1999b; Zhang & Fryer 2001), or a "failed supernova" or collapsar (Woosley 1993; MacFadyen & Woosley 1999), where a massive star collapses but produces a black hole instead of a neutron star at its center. These systems would produce a GRB by tapping the binding energy of the disc through neutrino emission (Goodman 1987; Jarozyński 1993; Jarozyński 1996; Witt et al. 1994; Thompson 1994; Mochkovitch et al. 1993; Mochkovitch et al. 1995; Popham, Woosley & Fryer 1999; Ruffert & Janka

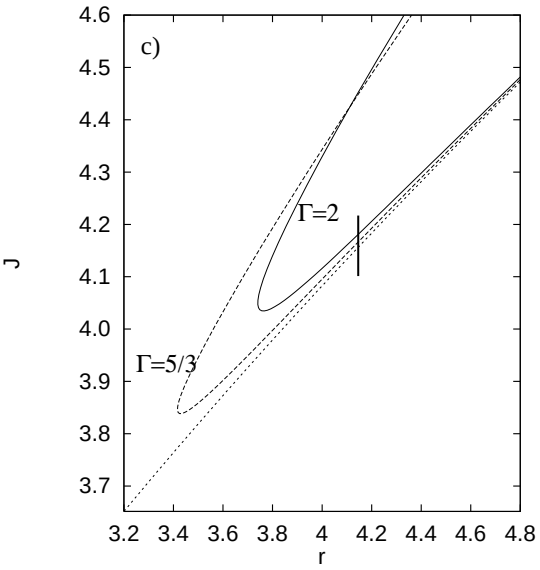

Figure 1. Total angular momentum as a function of binary separation for irrotational Roche–Riemann binaries using the method of LRSb for $\Gamma = 2$ (solid lines) and $\Gamma = 5/3$ (dashed lines) for (a) q=0.5; (b) q=0.31; (c) q=0.2. The dotted lines correspond to the solution computed for point masses in Keplerian orbits. The thick vertical lines mark the initial separations used for the dynamical runs.

1999), or the rotational energy of the black hole, through the Blandford & Znajek (1977) mechanism, producing so–called Poynting jets (Mészáros & Rees 1997b; Mészáros, Rees & Wijers 1999; Lee, Wijers & Brown 2000). Another class of models also involves neutron stars, but would power the GRB through the catastrophic release of rotational energy via intense magnetic fields (Usov 1992; Kluźniak & Ruderman 1998; Spruit 1999; Ruderman, Tao & Kluźniak 2000), or even through intense neutrino emission in a neutron star binary before the coalescence, because of tidal heating and compression (Salmonson, Wilson & Mathews 2001).

The ejection of neutron star matter to the interstellar medium during a dynamical coalescence might contribute to the abundances of heavy elements (Lattimer & Schramm 1974; Lattimer & Schramm 1976; Symbalisty & Schramm 1989; Eichler et al. 1989), in addition to the amounts expected from supernova explosions (Meyer & Brown 1997; Freiburghaus et al. 1999a). This question has been addressed in the numerical calculations of double neutron star mergers of Rosswog et al. (1999; 2000) and by Freiburghaus et al. (1999b). If the rates of black hole–neutron star mergers are comparable, it is possible that these systems might also contribute in the same way to the galactic abundances.

Our work on merging black hole–neutron star binaries began with low–resolution simulations (Lee & Kluźniak 1995) that used a stiff polytropic equation of state. The results initially led us to believe that, if proved true, these models were not likely to produce cosmological gamma ray bursts, because of excessive baryon contamination. We gradually increased our numerical resolution, using essentially Newtonian physics (except for our treament of gravitational radiation reaction, see below, § 2), and treated tidally locked binaries with stiff and soft equations of state (Lee & Kluźniak 1999a; Lee & Kluźniak 1999b, hereafter papers I & II), and irrotational binaries with a stiff equation of state (Lee 2000, hereafter paper III), always using a polytrope to model the initial neutron star. It became apparent early on that our initial suspicions were unfounded, and that indeed these systems were promising candidates for the central engines of GRBs (Lee & Kluźniak 1997; Kluźniak & Lee 1998). We also found that for very stiff equations of state (see papers I and III) the neutron star could avoid immediate tidal disruption, and that this would be reflected in the gravitational wave signal. Additionally, a substantial amount of mass could be ejected to the interstellar medium, and potentially undergo r–process nucleosynthesis, thus contributing to the abundances of heavy elements. Recently, Janka et al. (1999) used the same formalism that Ruffert et al. (1996; 1997) had employed for binary neutron star coalescence studies to simulate the merger of a black hole with a neutron star. Their calculations have revealed the same qualitative aspects of the process which we have found, with differences due mainly to the different formalism used for gravitational radiation reaction and their use of a different equation of state (Lattimer & Swesty 1991).

This paper is the last in the series that has used the approach briefly described above (and detailed below in § 2), having mapped the parameter space we intended to explore by varying the stiffness of the equation of state, the initial mass ratio in the binary and the distribution of angular momentum in the system (using tidally locked and irrotational binaries as initial conditions). A short exposition on the numerical method and initial conditions is given in § 2 and § 3 (for details concerning the implementation we refer the reader to the longer corresponding sections in paper III and the appendix in paper I), followed by our results in § 4. The effect different choices of initial conditions can have on the dynamical coalescence is presented in § 5, and a summary and discussion is given in § 6.

2 NUMERICAL METHOD

For the calculations presented in this work, we have used the method known as Smooth Particle Hydrodynamics (SPH) (see Monaghan 1992 for a review and Lee 1998 for a description of our own code). The code is the same one that was used for our previous simulations of irrotational black hole–neutron star binaries (paper III). Here we will not discuss the code in detail, but limit the presentation to a few basic points.

As before, the black hole is modeled as a Newtonian point mass of mass M_{BH} with an absorbing boundary at the Schwarzschild radius $r_{Sch} = 2GM_{\rm BH}/c^2$. Any SPH particle that crosses this boundary is absorbed by the black hole, whose mass and momentum are adjusted so as to ensure conservation of total mass and total linear momentum in the system.

The neutron star is modeled as a polytrope with a soft equation of state, so that the pressure is given by $P = K\rho^{\Gamma}$ with Γ and K being constants (see paper I). Unless otherwise noted, we measure mass and distance in units of the mass and radius of the unperturbed (spherical) neutron star (13.4 km and 1.4 $M_{\odot}$ respectively), so that the units of time,

density and velocity are

$$\tilde{t} = 1.146 \times 10^{-4}\mathrm{s} \times \left(\frac{R}{13.4\ \mathrm{km}}\right)^{3/2} \left(\frac{M_{\rm NS}}{1.4\ M_\odot}\right)^{-1/2} \quad (1)$$

$$\tilde{\rho} = 1.14 \times 10^{18}\mathrm{kg\ m^{-3}} \times \left(\frac{R}{13.4\ \mathrm{km}}\right)^{-3} \left(\frac{M_{\rm NS}}{1.4\ M_\odot}\right) \quad (2)$$

$$\tilde{v} = 0.39c \times \left(\frac{R}{13.4\ \mathrm{km}}\right)^{-1/2} \left(\frac{M_{\rm NS}}{1.4\ M_\odot}\right)^{1/2} \quad (3)$$

For the dynamical simulations presented here, we have used $N \simeq 80,000$ SPH particles to model the neutron star. The initial (spherical) polytrope is constructed by placing the SPH particles on a uniform three–dimensional grid with particle masses proportional to the Lane–Emden density. This ensures that the spatial resolution is approximately uniform throughout the fluid. This isolated star is then allowed to relax for a period of thirty time units (as defined above) by including a damping term linear in the velocities in the equations of motion. The specific entropies of the particles are kept constant during this procedure (i.e. K is constant in the equation of state $P = K\rho^\Gamma$).

To perform a dynamical run, the black hole and every SPH particle are given the velocity as determined from the corresponding initial condition (see below) in an inertial frame, with the origin of coordinates at the centre of mass of the system. Each SPH particle is assigned a specific internal energy $u_i = K\rho^{(\Gamma-1)}/(\Gamma-1)$ and the equation of state is changed to that of an ideal gas, $P = (\Gamma-1)\rho u$. The specific internal energy is then evolved according to the first law of thermodynamics, taking into account the contribution from artificial viscosity (see below). We vary the initial mass ratio $q = M_{\rm NS}/M_{\rm BH}$ in the binary by adjusting the mass of the black hole only.

Artificial viscosity is used in SPH to handle the presence of shocks and avoid particle interpenetration. As in paper III, we use the form of Balsara (1995), which vanishes in regions of large vorticity but retains the ability to deal with the presence of shocks (in regions of strong compression).

We include gravitational radiation reaction in the quadrupole approximation for point masses (Landau & Lifshitz 1975), with the same implementation as described in paper III. Namely, we apply a back reaction force to the black hole and the self–bound core of the neutron star, treating the latter as a point mass. The corresponding terms in the equations of motion are switched off once the star is tidally disrupted, when the core mass drops below 0.14 $M_\odot$. We continuously compute the radiation reaction time–scale $t_{RR}^{-1} = 256G^3 M_{\rm BH} M_{\rm core}(M_{\rm BH} + M_{\rm core})/(5r^4c^5)$ and an estimate of the current orbital period $t_{orb} = 2\pi/\sqrt{G(M_{\rm BH} + M_{\rm core})/r^3}$, where r is the separation between the black hole and the centre of mass of the core. For the typical separations and masses in the black hole–core binary, by the time the core mass has dropped to 0.14 $M_\odot$, the radiation reaction time–scale is much longer (by at least an order of magnitude) than the current orbital period.

3 INITIAL CONDITIONS

Exactly as for the results presented in paper III, we have used irrotational binaries for the dynamical runs shown here. This amounts to considering the stars have no spin in an external, inertial frame of reference. This initial condition is more realistic than that of a tidally locked binary, because the viscosity inside neutron stars is not large enough to maintain synchronization during the inspiral phase (Bildsten & Cutler 1992; Kochanek 1992). Essentially, the stars will coalesce with whatever spin angular momenta they have when the binary separation is large. Setting up accurate and self–consistent initial conditions in this case is not a trivial matter, and we use the same approximation as before. Namely, we apply the energy variational method of LRSb and take the neutron star to be a compressible tri–axial Roche–Riemann ellipsoid (see § 8 in LRSb).

We build an initial condition by first constructing a spherical star of given radius and mass, as described in § 2. We then use the method of LRSb to calculate the orbital angular velocity of the binary and the semimajor axes of the Roche–Riemann ellipsoid for the appropriate choice of adiabatic index, initial mass ratio and binary separation (see Table 1). The semimajor axes of the fluid configuration can also be calculated from the SPH numerical solution using

$$a_i = \sqrt{\frac{5I_{ii}}{\kappa_n M_{\rm NS}}}$$

where

$$I_{ii} = \sum_j m_j (x_j^i)^2.$$

The stiffness of the equation of state enters these equations through the parameter κ_n ($\kappa_n = 0.653$ for $\Gamma = 2$ and $\kappa_n = 0.511$ for $\Gamma = 5/3$). The first and second semimajor axes of the tri–axial ellipsoid lie in the orbital plane, with the first one along the line joining the two binary components. The third axis is oriented perpendicular to this plane (along the axis of rotation). The position of each SPH particle is then re–scaled (independently along each coordinate axis) so that the new fluid configuration has the appropriate semimajor axes. This ellipsoid is then used as an initial condition for the corresponding dynamical run. The initial velocity is given by the orbital angular velocity (for the azimuthal component) plus the radial velocity corresponding to point–mass inspiral. The variation in total angular momentum as a function of binary separation for irrotational Roche–Riemann binaries (with various mass ratios and adiabatic indices in the equation of state) is shown in Figure 1, as calculated using the method of LRSb. The curves show a turning point as the separation is decreased, indicating the presence of a dynamical instability in the system. Two distinctions are necessary at this point. First, the ellipsoidal approximation becomes less accurate as the separation is decreased. This applies regardless of the value of the adiabatic index, but is much more serious for stiff equations of state, because the tidal effects are more pronounced. Second, the adiabatic index does determine if the Roche limit (when mass transfer through overflow of the lobe occurs) is reached before or after the dynamical instability. For stiff equations of state (such as the ones shown in papers I & III), the instability can be reached at or before the Roche

limit. However, for a more compressible case (see paper II) the inverse occurs, and it is the mass transfer process itself (which is unstable) that is responsible for the subsequent evolution of the system.

We have chosen the values of the initial separation for our dynamical runs r_i to be slightly above the turning point (see Table 1). The ellipsoidal approximation is then still reasonable, and our equilibrium configurations have not yet reached the point where the neutron star will overflow its Roche lobe. When the dynamical simulation is initiated, the separation will decrease due to the emission of gravitational waves, and mass transfer will start promptly. The construction of full equilibrium initial conditions at the point of Roche lobe overflow is a problem that was addressed by Uryū & Eriguchi (1999).

The initial separations we have chosen are similar to what we have presented before for the case of tidally locked (papers I & II) and irrotational (paper III) black hole–neutron star binaries. We also include in Table 1 the initial parameters for two runs (C31S and D31S) that used initially spherical neutron stars for the dynamical calculations, with a Keplerian orbital angular velocity (as for runs A31S and B31S in paper III). We have performed these runs to gauge the effect non–equilibrium initial conditions will have on the evolution of the system, and show the results in § 5.

4 RESULTS

4.1 Morphology of the mergers

For every dynamical run, the decrease in binary separation leads to Roche lobe overflow on an orbital time–scale. A stream of gas forms at the inner Lagrange point, transferring matter from the neutron star to the black hole. At the same time, the star is tidally stretched and extends away from the black hole through the external Lagrange point. We show in Figures 2 and 3 density contours in the orbital plane at various times during the simulation for runs C31 and D31. For all other runs (C51, C31S, C20, D51, D31S and D20) the plots are qualitatively similar. As the accretion stream winds around the black hole, it collides with itself and forms a torus, while the gas thrown out through the outer Lagrange point forms a long tidal tail. For a the less compressible case ($\Gamma = 2$, run C31), the torus, as well as the tidal tail, are thinner, as one should expect. The accretion torus that is formed around the black hole is not initially azimuthally symmetric, but shows a double ring structure, particularly for $\Gamma = 2$ (see panels (d)–(h) in Figure 2). This appears as the gas that passes through periastron near the black hole overshoots the circular orbit that would correspond to the specific angular momentum it contains, forming an outer ring (see panels (c)–(d) in Figure 2). It then falls back towards the black hole and encounters the rear of the accretion stream. The subsequent collision tends to circularize the orbit of the fluid, and also pushes it to the inner ring, closer to the black hole (panels (d)–(e)). The structure of the outer ring rotates slowly counterclockwise (with the initial orbital motion) as the bulk of the tidally disrupted star (which produces the accretion stream) continues orbital motion in the same direction, on the opposite side of the black hole. At late times, the density contrast between the rings drops (see below, Figure 7(a) and (c), and Figure 10), but nevertheless a hump remains in the accretion disc, as there is still a visible stream feeding it from the oposite side. This structure was clearly seen for $\Gamma = 2.5$ in the results presented in paper III, and for the same reasons. It is present as well for $\Gamma = 5/3$ (see Figure 3), although the distinction between having two rings and a hump is not as marked, even as the disc is forming (panels (c)–(e)). This is due to the higher compressibility of the material, and hence its tendency to expand at low densities. At late times the disc is much more azimuthally symmetric than for $\Gamma = 2$ (see below Figure 7(b) and (d)).

Our implementation of gravitational radiation reaction is valid only for circular orbits. Thus we monitor the eccentricity e of the orbital motion during the coalescence, to ensure that it remains small before gravitatational radiation reaction is switched off. We compute an estimate for e by assuming that it is that of a binary system with masses $M_{\rm BH}$ and $M_{\rm core}$, given by $e = \sqrt{1 + 2EJ^2/G^2\mu M_{\rm core}^2 M_{\rm BH}^2}$, where $\mu = M_{\rm core}M_{\rm BH}/(M_{\rm core} + M_{\rm BH})$, and E and J are the mechanical energy and angular momentum of the orbital motion. During the initial phase, $e \approx 0.05$, and close to the instant of minimum binary separation (at $t \simeq 20$ for most runs) $e < 0.1$. By the time radiation reaction is switched off (at $t \simeq 30$, see Table 1), the eccentricity has increased somewhat, to $e \simeq 0.2$. At this stage the mass ratio (between the core and the black hole) has dropped enough so that the effects of including radiation reaction are very small.

The separation between the centre of mass of the core and the black hole is shown in Figure 4 for all runs. Initially, it decreases at a rate consistent with that of a point–mass binary, and subsequently does so at an even faster rate, due to hydrodynamical effects. This is particularly important for high mass ratios ($q = 0.5$ and $q = 0.31$). For $q = 0.2$, the deviation is smallest and almost negligible, until $t \approx 13-15$, depending on the value of Γ. Once the initial mass transfer episode is under way, the separation reaches a minimum and then increases, as the core of the star is stretched and moves to a greater separation. Qualitatively, the evolution resembles that of a stiff equation of state (paper III) except that now the point–mass approximation for the orbital decay is valid for a longer time (at smaller separations for a given value of q, compare for example the case with $q = 0.2$ in the two panels in Figure 4). This is simply due to the fact that the stars are better approximated by point masses as the adiabatic index is decreased. The point at which the separation is at a minimum coincides with the maximum accretion rate (see below). After this initial periastron passage, the star is completely disrupted, and in every case the final configuration consists of a massive accretion disc around the black hole. Gravitational radiation reaction is switched off at $t \approx 30$ for all runs (see Table 1) when the core mass drops below 0.14 $M_\odot$.

As mentioned above, the material which moves away from the black hole through the outer Lagrange point forms a long one–armed spiral in the system. This structure is usually formed during a dynamical coalescence (it is a two–armed spiral in the case of neutron star mergers, with each star producing one arm, see e.g. RS94). The main difference between the runs presented here and the case of low compressibility studied in paper III is that no clumps are formed, and the distribution of matter remains smooth along the

Table 1. Basic parameters for each run. The table lists for each run (labeled) the initial mass ratio, the adiabatic index used, the initial orbital separation, the axis ratios for the tri–axial ellipsoid used as an initial condition, the initial orbital angular velocity of the binary, the time at which gravitational radiation reaction is switched off in the simulation, the time at which the simulation was stopped, and the initial number of particles. The runs labeled C31S and D31S used an initially spherical neutron star (otherwise irrotational Roche–Riemann ellipsoids were used, see text for details).

Run	q	Γ	r_i	a_2/a_1	a_3/a_1	$\tilde{\Omega}$	t_{rad}	t_f	N
C50	0.50	2.0	3.25	0.842	0.857	0.29753	35.12	200.0	81,608
C31	0.31	2.0	3.70	0.828	0.844	0.29042	35.80	200.0	81,608
C31S	0.31	2.0	3.70	1.000	1.000	0.28881	34.76	200.0	81,608
C20	0.20	2.0	4.15	0.808	0.826	0.29117	30.12	200.0	81,608
D50	0.50	5/3	3.25	0.904	0.911	0.29644	37.03	200.0	82,136
D31	0.31	5/3	3.60	0.884	0.892	0.30182	30.40	200.0	82,136
D31S	0.31	5/3	3.60	1.000	1.000	0.30094	29.44	200.0	82,136
D20	0.20	5/3	4.15	0.884	0.892	0.29037	26.96	200.0	82,136

length of the tail (as observed also in paper II, RS92, RS95 for soft equations of state).

We show in Figure 5 the accretion rates onto the black hole for runs C50, C31, C20, D50, D31 and D20. The maximum rates are reached during the initial episode of Roche lobe overflow ($\dot{M}_{max} \approx 0.06 - 0.09$, equivalent to $0.7 - 1.1\ M_\odot\ \mathrm{ms}^{-1}$). They correspond mainly to matter that is directly accreted by the hole from the mass transfer stream coming from the neutron star. As the accretion disc is formed around the black hole, $\dot{M}$ gradually decreases, although there are small oscillations. One can see in the curves that there are secondary maxima in $\dot{M}$ at $t < 60$ for all runs. This is due to the circularization process of the orbits in the disc. The streams of matter coming from the neutron star collide with themselves, and some matter (along the inner edge of the stream) falls onto the black hole with greater ease, giving rise to the quasi–periodic oscillations in the accretion rate. This only occurs two or three times at most, and at late times ($t \geq 100$) the accretion rate is decreasing monotonically, showing the circularization of the orbits. These peaks are present in the runs shown in paper III, but the lower resolution used there makes it harder to appreciate them.

The peak accretion rates shown in Table 2 are substantially higher when $\Gamma = 5/3$, by up to a factor of $\simeq 1.4$ for $q = 0.2$. This is one of many effects of the mass–radius relationship that are observed during dynamical coalescences. For polytropes, $R \propto M^{\Gamma-2/(3\Gamma-4)}$, so for $\Gamma = 2$ the stellar radius is unaffected by mass loss (or accretion), while for $\Gamma = 5/3$, $R \propto M^{-1/3}$ and thus the star will expand upon overflowing its Roche lobe and losing mass. The decrease in separation due to energy losses to gravitational waves is what initially brings the star to the point of Roche lobe overflow. The star's reaction when this happens then depends on the compressibility. When $\Gamma = 2$, the effect of tidal forces and gravitational wave back reaction are enough to completely disrupt the star. For $\Gamma = 5/3$, there is an added, runaway effect, because since the star *expands* upon losing mass, it further overflows its Roche lobe (and thus produces higher accretion rates). This alone can de–stabilize the orbit and induce coalescence, as observed for the case of a tidally locked system with $\Gamma = 5/3$, *without* gravitational wave back reaction (this was done initially as a test and reported in paper II). This also explains why the total disc mass is lower for a given initial mass ratio for $\Gamma = 5/3$ (also given in Table 2, column 2).

The total angular momentum in the system decreases for two reasons. First, there is a decay due to the emission of gravitational waves (seen at early times before substantial mass transfer has taken place), and second, much of the angular momentum of the accreted matter is lost to the spin of the black hole. As stated above, when accretion occurs we update the mass and momentum of the black hole so as to ensure conservation of total mass and linear momentum. Conservation of angular momentum then allows us to estimate the degree to which the black hole is spun up as a result of accretion, and we calculate its Kerr parameter $a = J_{\rm BH}c/GM_{\rm BH}^2$ at the end of the simulation (we take $a = 0$ at $t = 0$). This is shown in column 8 of Table 2. We note that our previously published results for a in papers II and III contained an error which we have now corrected. An explanation and the correct values are given in the appendix. For a fixed adiabatic index, the black hole is spun up to a greater degree (up to almost one half the maximum rotation rate) at higher mass ratios, simply because it is less massive. The higher rotation rates seen at lower Γ reflect the corresponding higher accretion rates (see above) and the fact that the total accreted mass is greater.

The various energies in the system are shown in Figure 6 for runs C31 and D31. The changes in mechanical energy seen at early times are due to the back reaction of gravitational waves, while the initial episode of mass transfer in the initial stages of the coalescence is evident in the large changes that occur at $t \approx 15$. At later times, the variation is small and the curves show a monotonical decay as the accretion discs become more azimuthally symmetric.

The core of the neutron star moves away from the black hole for the same reasons as outlined in paper III for the case of a stiff equation of state. In the case of conservative mass transfer (where the total mass and orbital angular momentum J are conserved), if the donor is the less massive component, the binary separation will increase. The system is not strictly conservative in this case, but the global response is the same. The specific angular momentum in the core increases as mass transfer proceeds, and this makes the separation increase. The mass–radius relationship outlined above makes it impossible for the system to survive as a stable binary, as was the case for $\Gamma = 3$ (paper III). As soon as the star overflows its Roche lobe, catastrophic mass transfer ensues, completely disrupting the star. The two dominant effects as far as the orbital evolution is concerned are the gravitational wave emission (and the accompanying loss of angular momentum) and mass transfer. In the cases shown here, (where the neutron star expands or maintains a con-

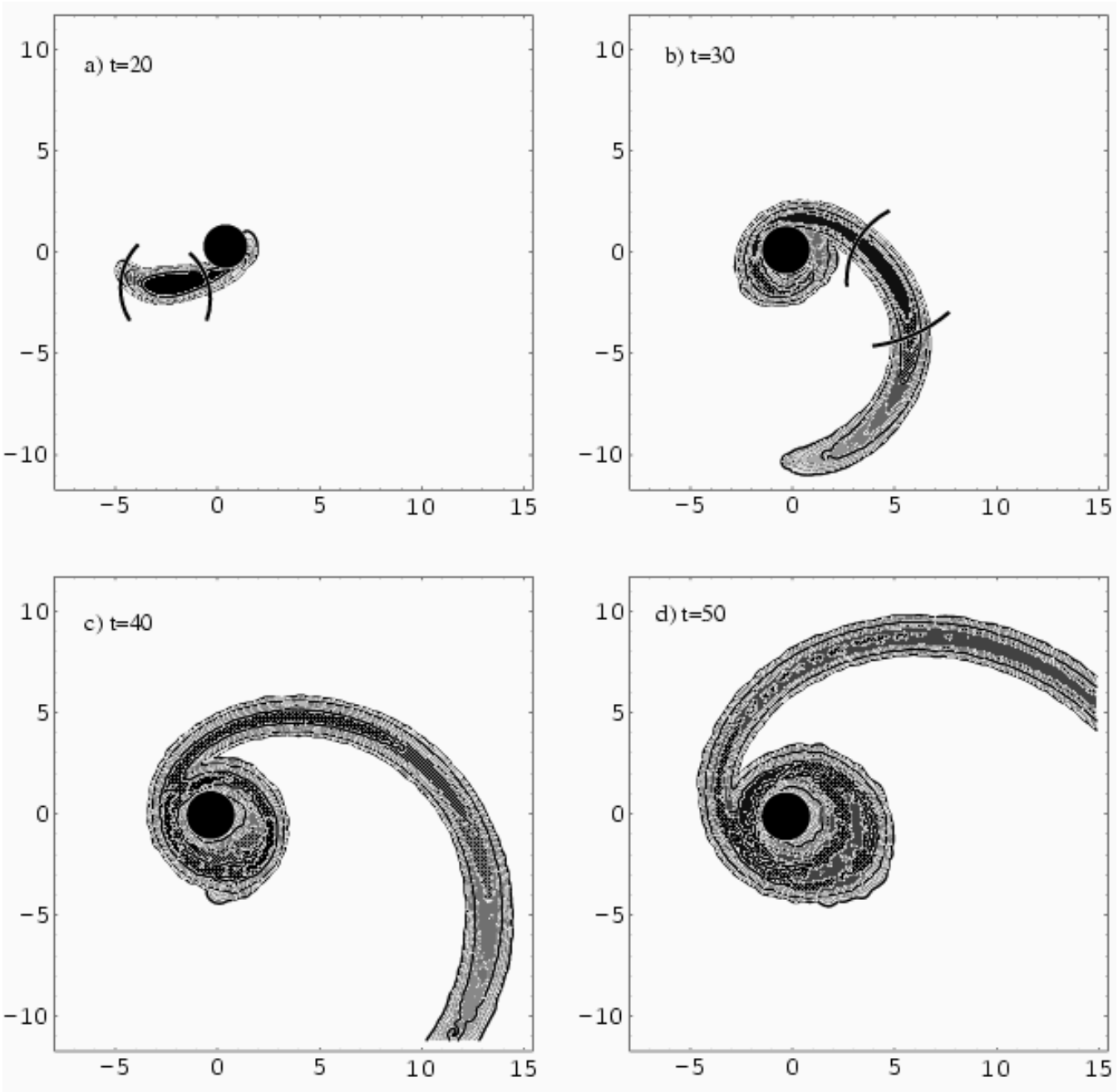

Figure 2. Density contours in the orbital plane during the dynamical simulation of the black hole–neutron star binary with initial mass ratio $q = 0.31$ and $\Gamma = 2$ (run C31). The orbital rotation is counterclockwise. All contours are logarithmic and equally spaced every 0.25 dex. Bold contours are plotted at $\log \rho = -4, -3, -2, -1$ (if present) in the units defined in eq. 2. The thick black arcs bound the matter that forms the core (see § 2). The time for each frame is given in the units defined in eq. 1.

stant radius upon losing mass), both effects lead to complete tidal disruption of the star on an orbital time–scale. For a stiff equation of state they tended to drive the system in opposite directions, with angular momentum losses making the separation decrease while mass transfer increased it. The outcome in that case was *episodic* mass transfer, and the frequent formation of accretion discs when the star was disrupted. Thus, in the present case as well, *stable* mass transfer from the neutron star is impossible, and the final configuration consists of a massive accretion disc around the black hole.

4.2 Accretion disc structure

In Table 2 we show several parameters related to the accretion structure around the black hole at the end of the simulation. The disc masses are computed as before (papers II and III), by taking into account the mass which has specific angular momentum $j > \sqrt{6}GM_{total}/c$, so that it will remain in orbit around the black hole. This means that only a fraction f of the gas mass left in the system at the end of the simulation is considered for the accretion tori (usually around 70%, the specific value of f for each run is given in

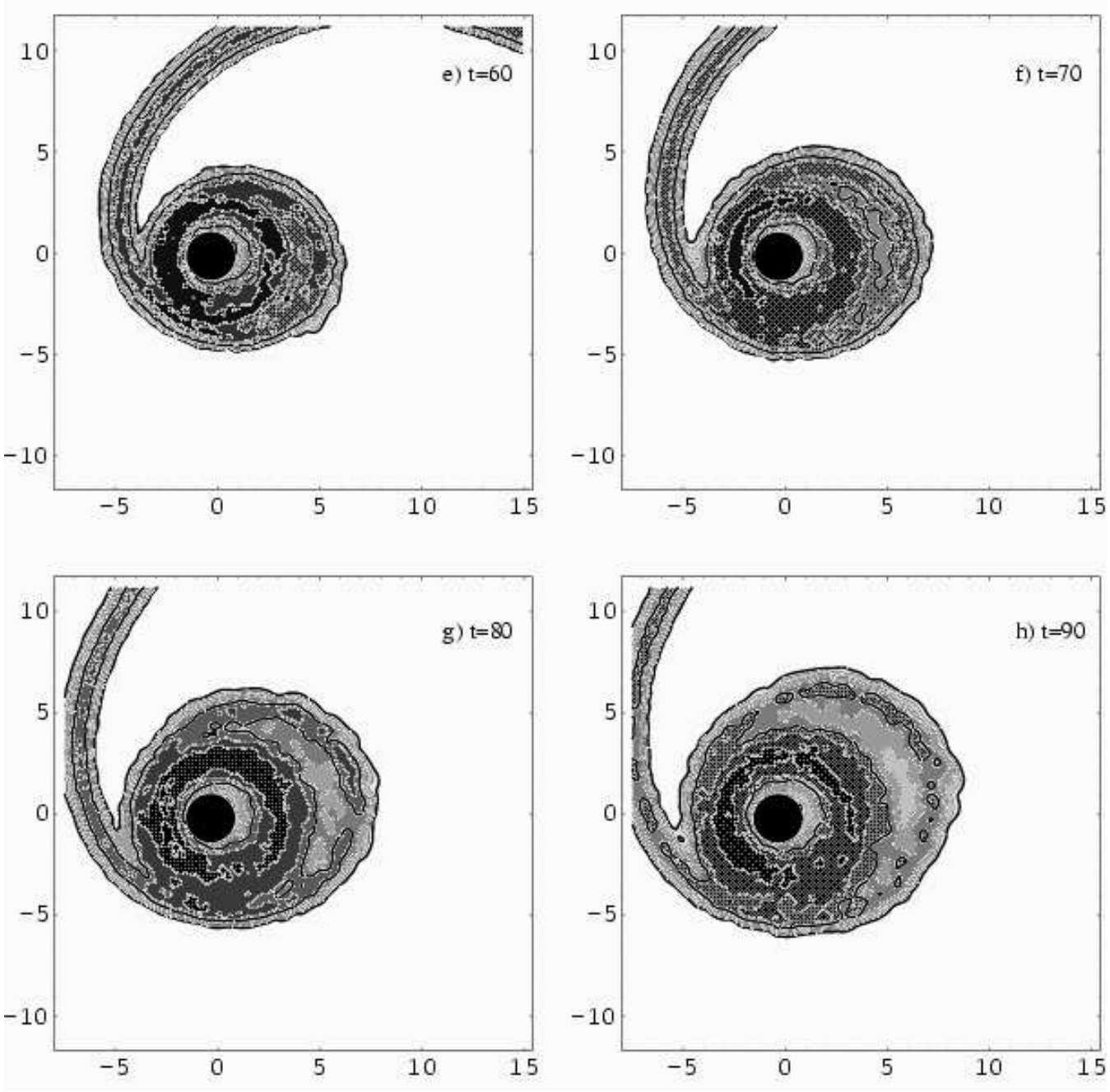

Figure 2. continued

the third column of Table 2). The disc masses are lower at lower Γ (as mentioned above) and at a lower initial mass ratio, but there is always at least 0.1 solar masses left in a debris torus. From the final accretion rate (comparable in every case) and the disc mass at $t = t_f$ we infer a rough estimate of the lifetime of the disc, which is beteen 30 and 70 ms. Since it is viscosity that drives the evolution of the disc at late times, and hence in this case a purely numerical effect, these values should be taken only as a guideline. The true lifetime of the disc depends on the redistribution of angular momentum through viscous effects and possibly dynamical instabilites. The former would probably make for a longer–lived disc, while the latter would tend to act in the opposite direction.

The double ring structure mentioned above gradually disappears as the density contrast between the rings drops, and the disc becomes more azimuthally symmetric as the simulation progresses. By $t = t_f$ it is meaningful to take azimuthal averages of quantities such as the density, internal energy and specific angular momentum in the disc. These are shown in Figure 8 for runs C31 and D31 (the corresponding plots for the remaining runs are quite similar). The density has a maximum at a characteristic distance r_0, which is between 50 and 70 km. (Another estimate of the lifetime of the disc can be obtained by evaluating $|r_0/v_r|$,

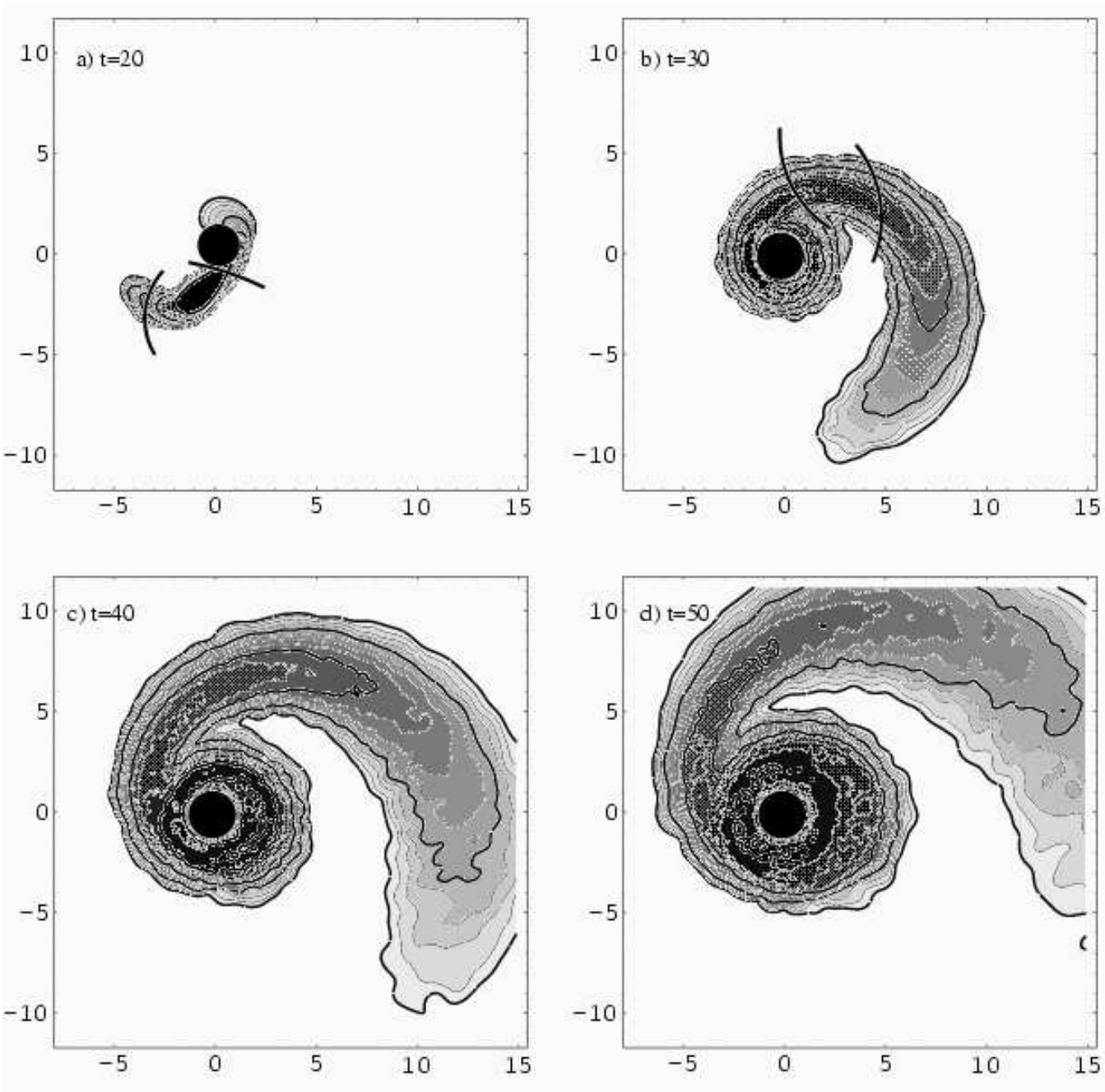

Figure 3. Density contours in the orbital plane during the dynamical simulation of the black hole–neutron star binary with initial mass ratio $q = 0.31$ and $\Gamma = 5/3$ (run D31). The orbital rotation is counterclockwise. All contours are logarithmic and equally spaced every 0.25 dex. Bold contours are plotted at $\log \rho = -5, -4, -3, -2, -1$ (if present) in the units defined in eq. 2. The thick black arcs bound the matter that forms the core (see § 2). The time for each frame is given in the units defined in eq. 1.

where v_r is the radial (inward) velocity of the fluid at r_0. The resulting lifetimes τ_{infall} are of the same order as those shown in Table 2.) The specific internal energies are maximum in the inner regions of the discs, and the profiles flatten out at $r \approx 2r_0$, at about $u/1000 = 2 \times 10^{-5}$, equivalent to 3×10^{18} erg g^{-1}, or 3 MeV nucleon^{-1}. The rotation curves are subkeplerian, indicating that pressure support is important. The slight increase in the curves of specific angular momentum seen in Figure 8b at $r \approx 10$ (particularly for $\Gamma = 2$) are due to the persistent outer ring in the accretion disc (see Figure 7). The slow drop in specific angular momentum for $r > 10$ marks the edge of the accretion disc at $t = t_f$. We note that in the inner regions, where the orbits have been circularized through the dynamical process mentioned above, the rotation curves are always close to, and below the Keplerian value. The torus does *not* have a

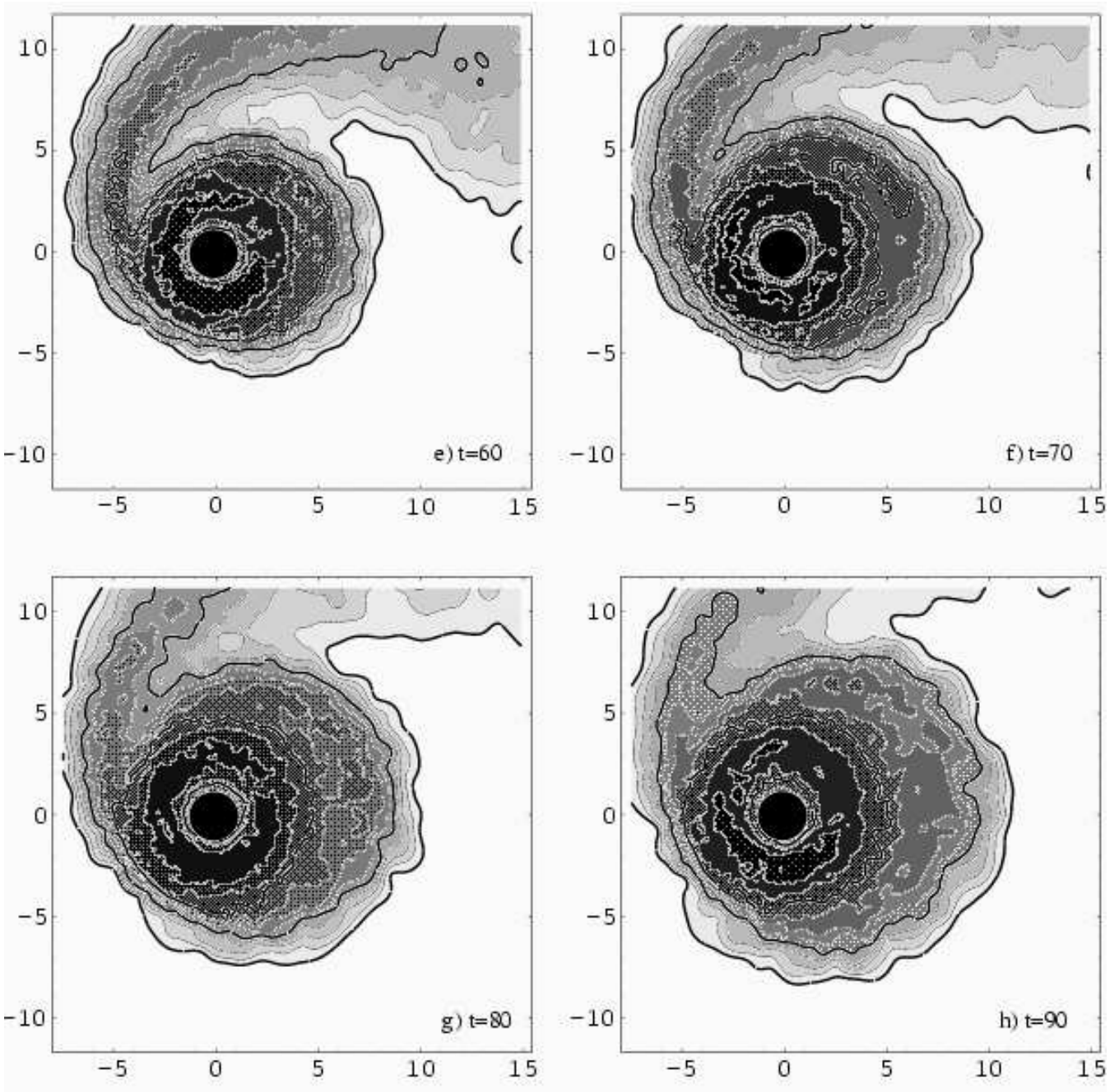

Figure 3. continued

constant distribution of specific angular momentum j, even immediately after being formed.

Since one of our main motivations for this line of work has been the production of cosmological gamma ray bursts from theses systems, we show as usual the distribution of matter along the rotation axis. This is the region where the densities are lowest, and from which a relativistic fireball could possibly emerge from the system and produce a GRB. This could possibly be powered by neutrino emission from the disc and subsequent pair production and expansion, or through the Blandford & Znajek (1977) mechanism, by tapping the energy stored in the spin of the black hole (see Table 2). In order for this to occur, the baryon loading must be small (on the order of $10^{-5}M_{\odot}$), so that the expansion can occur at the required Lorentz factors $\Gamma \geq 10^2$ (Mészáros & Rees 1992; Mészáros & Rees 1993). In Figure 9 we show the baryon contamination along the rotation axis by plotting the amount of mass enclosed in a cone with opening angle $\Delta\theta$ above and below the black hole and along the rotation axis (see also the last three columns in Table 2). Clearly, only modest collimation is required (of about 10°) to stay below the $10^{-5}M_{\odot}$ threshold mentioned above. This is a

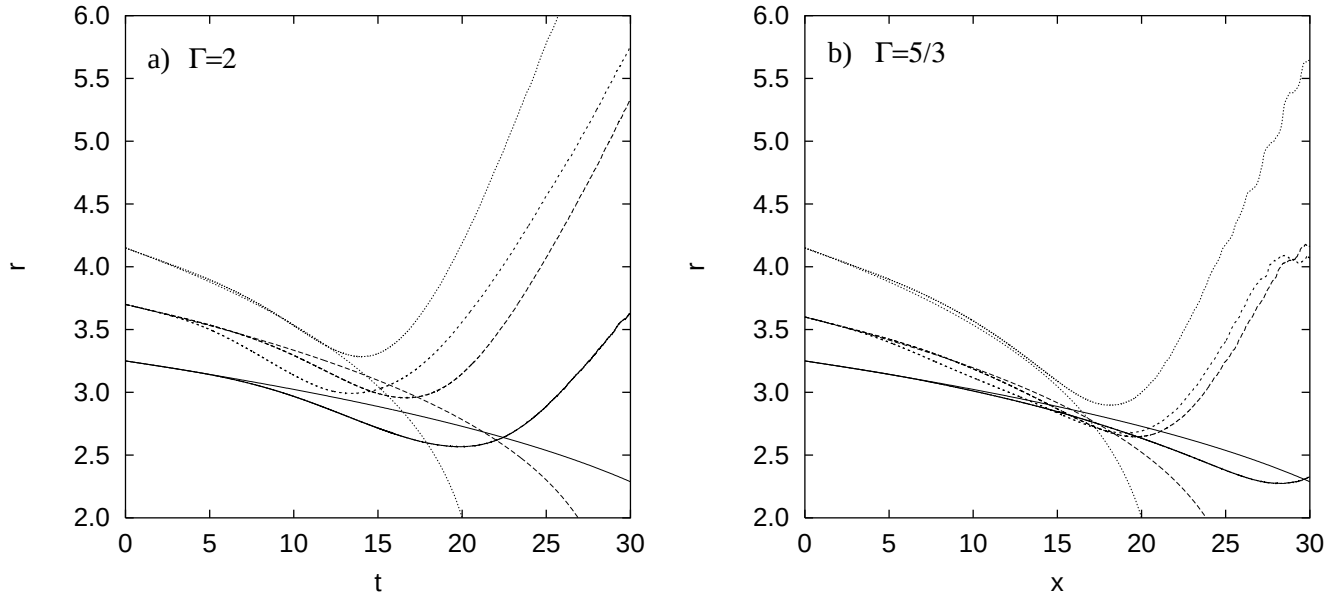

Figure 4. Separation between the black hole and the centre of mass of the core (see § 2) for (a) $\Gamma = 2$ and (b) $\Gamma = 5/3$ (runs C50 and D50—solid lines; runs C31 and D31—long–dashed lines; runs C31S and D31S—short–dashed lines; runs C20 and D20–dotted lines). For $q = 0.31$ there are two curves in each frame, corresponding to runs initiated with a spherical polytrope and an irrotational Roche–Riemann ellipsoid. In both cases, the one that decays faster corresponds to the former condition. The monotonically decaying curves correspond to point–mass binaries with the same initial separation and mass ratio, evolving through gravitational wave emission, computed in the quadrupole approximation.

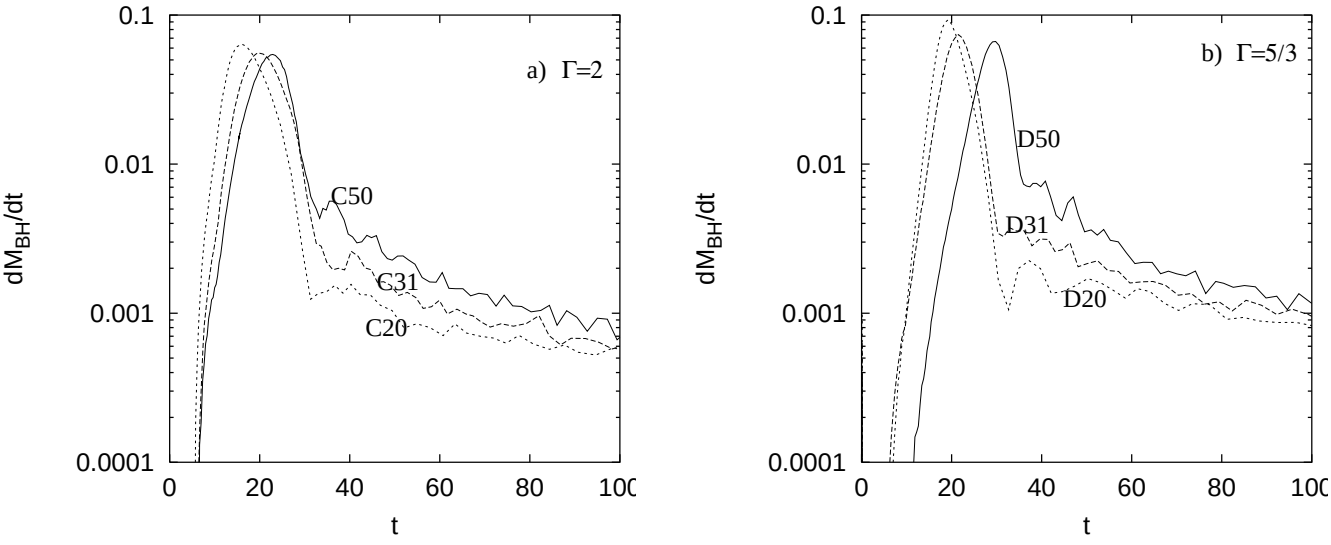

Figure 5. Mass accretion rate onto the black hole for (a) $\Gamma = 2$ and (b) $\Gamma = 5/3$. The curves are plotted only for $t < 100$, at later times there is little further evolution as $\dot{M}$ decreases monotonically.

fact that has become clearer in our simulations as we have increased the resolution, from 8,000 SPH particles for the majority of the runs shown in paper I to the 80,000 particles used for the simulations shown here (in increasing the number of particles by an order of magnitude, the spatial resolution increases by a factor of $\simeq 2.15$).

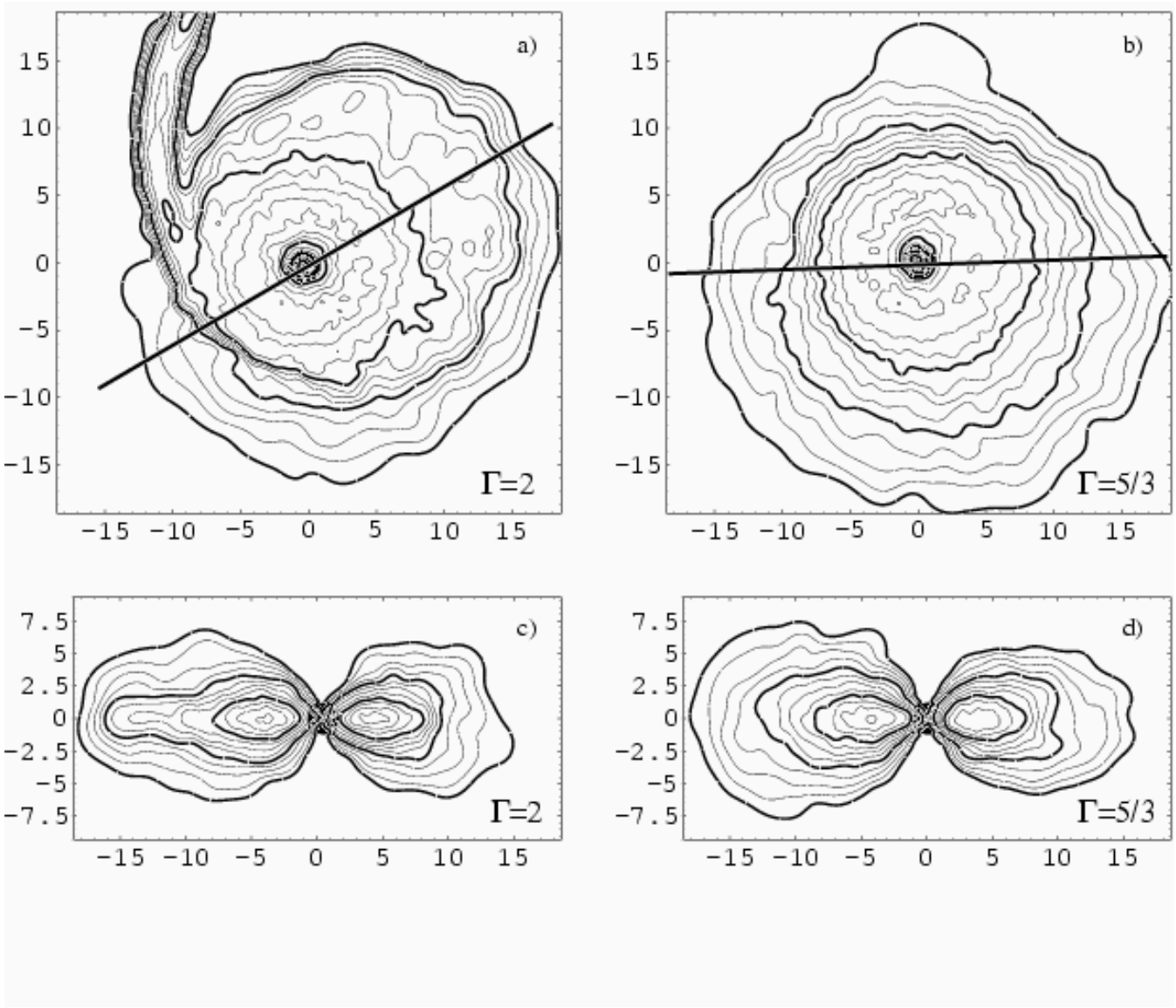

Figure 7. Density contour plots at $t = t_f$ for runs C31 (a,b) and D31 (c,d) in: (a,c) the orbital plane; (b,d) the meridional plane shown by the black line in panels (a,c). All contours are logarithmic and equally spaced every 0.25 dex. Bold contours are plotted at $\log \rho = -6, -5, -4$ (if present) in the units defined in eq. 2.

Table 2. Accretion disc structure. In the last three columns, θ_{-n} is the half–angle of a cone above the black hole and along the rotation axis of the binary that contains a mass $M = 10^{-n}$. The mass is given in units of 1.4 $M_\odot$, and time is measured in the units defined in equation 1.

Run	M_{disc}	f	$\dot{M}_{max}$	$\dot{M}_{final}$	$M_{ejected}$	τ_{disc}	$J_{\rm BH}c/GM_{\rm BH}^2$	θ_{-3}	θ_{-4}	θ_{-5}
C50	0.181	0.71	0.054	$3{\cdot}10^{-4}$	$0.48{\cdot}10^{-3}$	603	0.334	41	25	15
C31	0.172	0.71	0.057	$3{\cdot}10^{-4}$	$10.20{\cdot}10^{-3}$	573	0.234	46	30	18
C31S	0.179	0.73	0.053	$3{\cdot}10^{-4}$	$11.51{\cdot}10^{-3}$	596	0.232	48	30	18
C20	0.138	0.59	0.065	$3{\cdot}10^{-4}$	$6.97{\cdot}10^{-3}$	460	0.162	52	38	25
D50	0.159	0.19	0.067	$3{\cdot}10^{-4}$	$0.21{\cdot}10^{-4}$	530	0.343	35	19	12
D31	0.141	0.63	0.074	$3{\cdot}10^{-4}$	$0.80{\cdot}10^{-4}$	470	0.242	43	26	12
D31S	0.144	0.64	0.072	$3{\cdot}10^{-4}$	$2.14{\cdot}10^{-4}$	480	0.241	46	26	13
D20	0.086	0.50	0.094	$3{\cdot}10^{-4}$	$0.05{\cdot}10^{-4}$	286	0.172	51	35	22

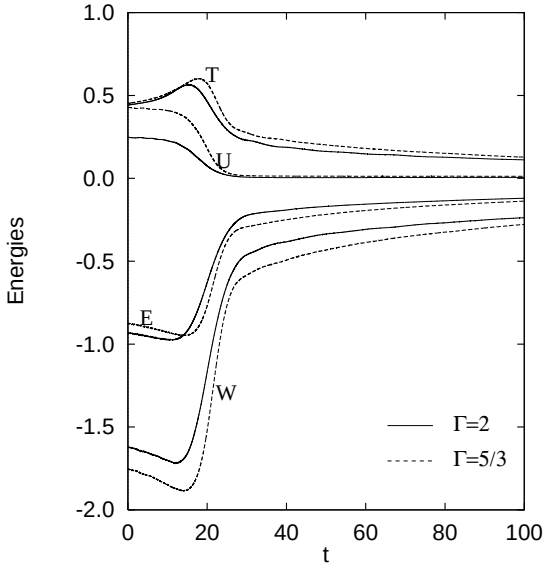

Figure 6. Energies in the system as a funcion of time for $q = 0.31$ (runs C31 and D31). The kinetic (T), total internal (U), gravitational potential (W) and total (E) energies are given in units of 3.8×10^{53} erg.

4.3 Ejected mass

During the initial encounter, a tidal tail of material stripped from the neutron star is formed in every dynamical run. This tail has been observed before for a stiff equation of state (paper III), where it persists as a well–defined structure throughout the simulations. For the cases studied here, it is present for $\Gamma = 2$ (see Figure 10), but essentially disappears as a coherent structure at late times for $\Gamma = 5/3$, as the density drops and the tail expands. We have calculated the amount of dynamically ejected mass for every run as before, computing the total mechanical energy (kinetic+gravitational potential) of the fluid, and counting as ejected that mass for which it has a positive value at $t = t_f$. There are two distinct categories of ejected mass during the simulation. The first (type I) corresponds to matter *dynamically* ejected from the system, and can be found in the orbital plane, at the tips of the tidal tails formed during the disruption of the star at early times ($t < 30 - 40$, see panels (b)–(d) in Figures 2 and 3, and Figure 10). The second (type II) comes from the surface of the accretion disc, and is ejected from the system at later times ($t > 70$). Ejected matter of type II only appears in a significant amount for the runs with $\Gamma = 5/3$, and is mainly of numerical origin, as it is the equation of state that models more compressible gas. This means that the fluid expands to occupy a larger volume than for less compressible equations of state. Thus for a given number of SPH particles, the spatial resolution is lower (i.e. the smoothing length h is larger), particularly at the edge of the matter distribution, and the effects of heating due to the artificial viscosity can be more pronounced. It was not mentioned in paper III simply because no resolvable amount of mass was ejected in this fashion. For $\Gamma = 2$ it amounts to only a tiny fraction of the total ejected mass (and a handful of particles). For $\Gamma = 5/3$ however, this is no longer true. In fact, most of the ejected matter is type II in this case. We have not counted it in the values tabulated in the sixth column of Table 2, keeping only type I ejected matter. Including the internal energy u of the fluid does not alter the results given, since the gas coming from the tips of the tidal tails has not been subjected to strong compression and heating, as it was never part of the accretion torus around the black hole.

For the softer equation of state, mass ejection is strongly suppressed, by approximately two orders of magnitude. This effect is so strong that for run D20 only about 20 SPH particles leave the system. This is similar to what was observed by Rosswog et al. (1999) in the case of double neutron star mergers. The underlying reason is that as the adiabatic index is lowered, the star becomes more centrally condensed, and thus the gravitational potential well becomes progressively deeper. For polytropes, the gravitational potential and the density are related by $\Phi = -K_\Gamma \Gamma/(\Gamma - 1)\rho^{\Gamma-1}$ where K_Γ depends on the value of Γ. This gives $\Phi_c(\Gamma = 2) = 0.74\Phi_c(\Gamma = 5/3)$, at a constant stellar mass and radius. This alone makes it more difficult to extract gas from the stellar potential well, through the gravitational interaction with the black hole during coalescence and eject it from the system. In all simulations, we see that the gas that is dynamically ejected (type I) comes from the surface layers of the star. So if the potential well is deeper, less matter is available for this sort of ejection, all other things being equal. There are at least three more effects that enhance this result and tend to decrease the amount of ejected mass at higher compressibilities. The first is that more violent events (as measured for example by the departure from point–mass behavior at small separations, see Figure 4) tend to eject more matter. Since these deviations are driven precisely by hydrodynamical effects, their influence is reduced at low Γ. Second, as pointed out above, the ejected matter comes from the surface layers of the star, and thus from regions that are at lower density at low values of Γ, making for less total matter available for ejection. Third, as can be seen in Figure 1, there is less total angular momentum in the system as Γ is decreased (also due to a greater degree of central condensation in the star), and so it will be more difficult for matter to escape the system in that case.

The combination of the effects mentioned above makes for a dramatic drop in the value of $M_{ejected}$ given in Table 2 as a function of Γ. The transition is sharp, due to the gradual increase in central condensation of the star, and in particular to the qualitative change in the mass–radius relationship that occurs at $\Gamma = 2$.

4.4 Emission of gravitational waves

The waveforms and luminosities are calculated in the quadrupole approximation from the values of the reduced moment of inertia tensor, and its time derivatives, see e.g. Finn (1989) and RS92. One polarization of the waveforms is shown in Figure 11 for runs C31 and D31, compared with the result for point masses decaying in the same approximation, and the corresponding luminosities are plotted in Figure 12. The results are very similar for the dynamical runs with a different initial mass ratio (runs C50, D50, C20 and D20).

The tidal disruption of the neutron star in every run (irrespective of the mass ratio) after the first episode of mass transfer following periastron passage, makes the am-

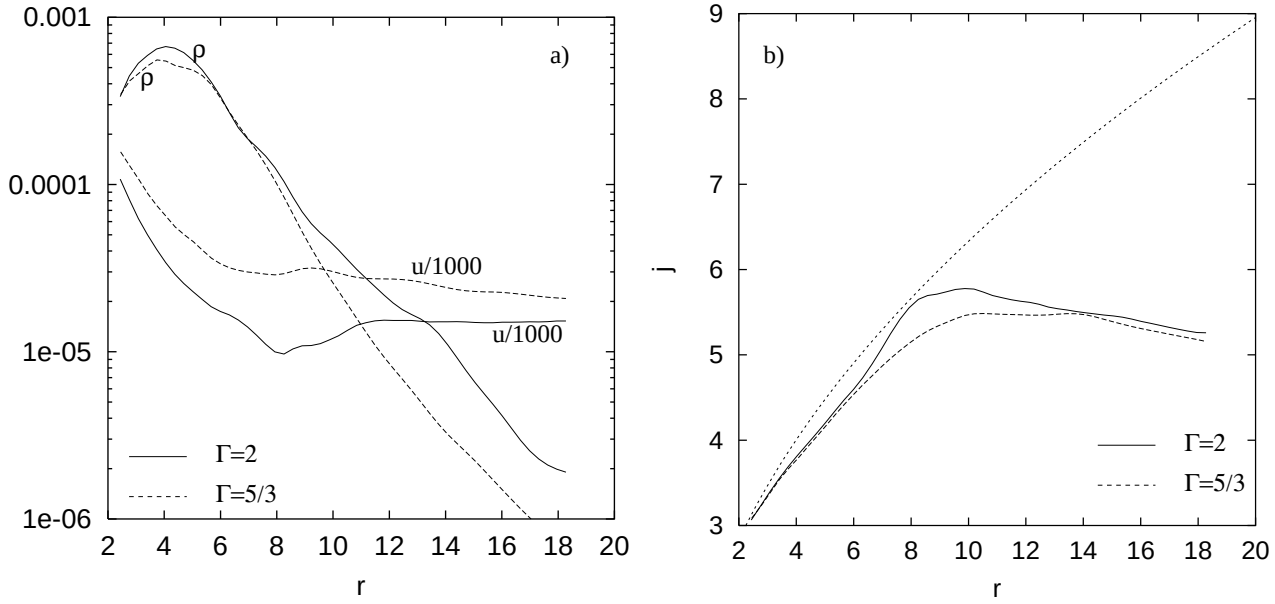

Figure 8. (a) Azimuthally averaged profiles for the density ρ and internal energy u ($u/1000$ is plotted) for runs C31 ($\Gamma = 2$) and D31 ($\Gamma = 5/3$) in the equatorial plane at $t = t_f$. (b) Specific angular momentum j in the equatorial plane for the same runs as in (a). The monotonically increasing curve corresponds to that of a Keplerian accretion disc around a black hole of the same mass (the mass of the black hole at $t = t_f$ for runs C31 and D31 differs by less than 1 per cent).

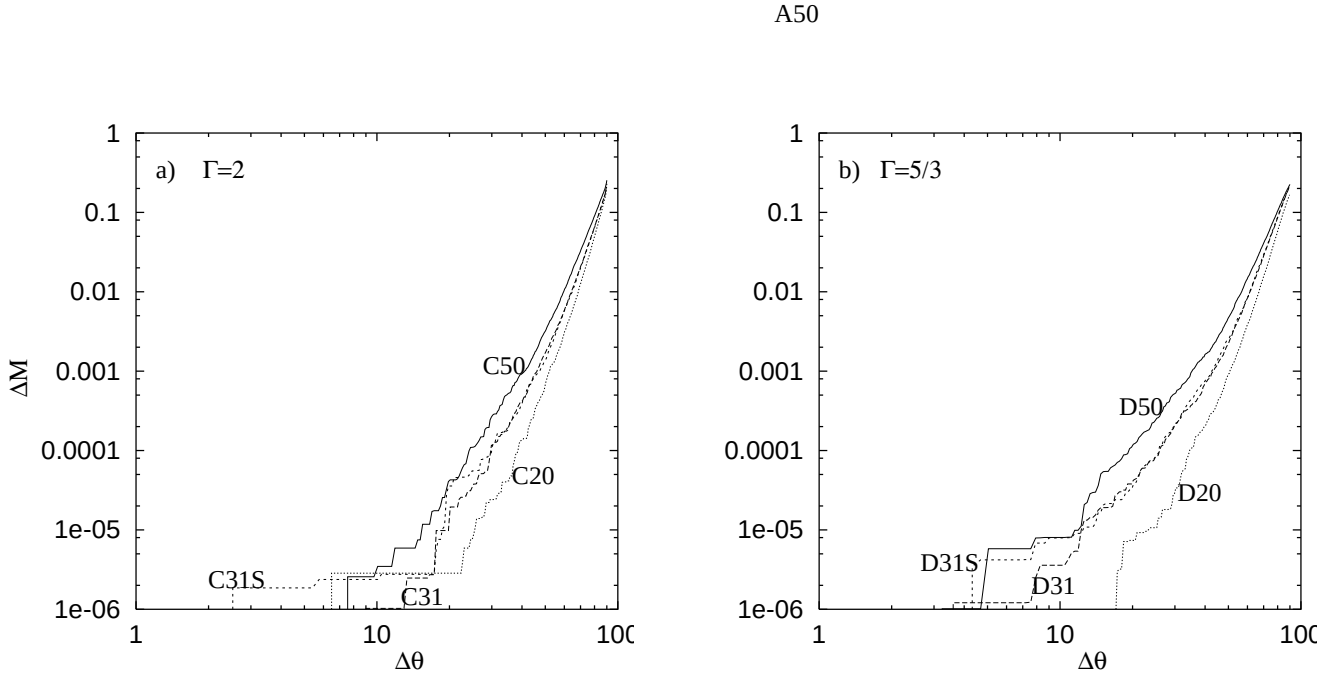

Figure 9. Enclosed mass for all runs as a function of half–angle $\Delta\theta$ (measured from the rotation axis in degrees) for (a) $\Gamma = 2$ and (b) $\Gamma = 5/3$ at $t = t_f$.

plitudes of the waveforms drop abruptly, and practically to zero, as the accretion torus is formed and becomes ever more azimuthally symmetric. Upper bounds for the final amplitude (at $t = t_f$) are shown in Table 3, where we show the maximum and final amplitudes for the waveforms, the peak luminosity and the total energy radiated away by the system, and the efficiency of gravitational wave emission $\epsilon = \Delta E/M_{\rm total}c^2$. For reference, $L_{max} = 1$ (in the units given in the table) corresponds to 3.036×10^{55} erg s^{-1}and $\Delta E = 10$ is equivalent to 3.48×10^{52} erg. The one–armed

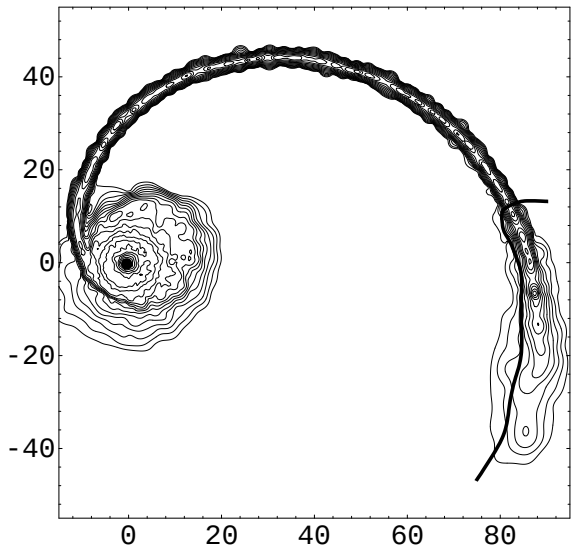

Figure 10. Density contours in the orbital plane at $t = t_f$ for run D31. All contours are logarithmic and equally spaced every 0.25 dex. Bold contours are plotted at $\log \rho = -6, -5, -4$ in the units defined in eq. 2. The thick black line across the tidal tail divides the matter that is bound to the black hole from that which is on outbound trajectories.

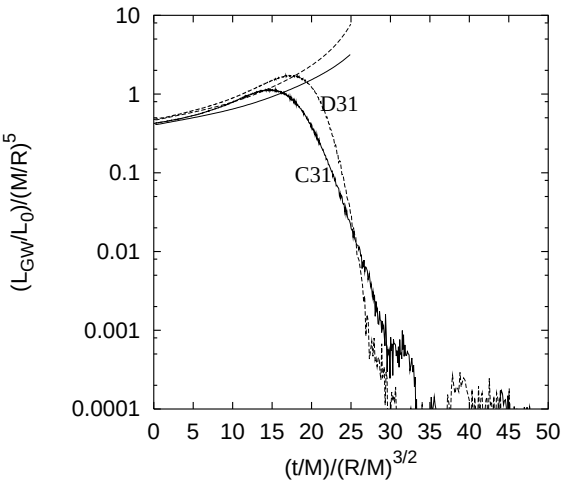

Figure 12. Gravitational radiation luminosity for the same runs as shown in Figure 11 (solid lines, run C31; dashed lines, run D31). The monotonically increasing curves show the corresponding result for a point–mass binary with the same initial mass ratio and separation, decaying in the quadrupole approximation. All quantities are given in geometrized units such that $G = c = 1$ ($L_0 = c^5/G = 3.64 \times 10^{59}$ erg s^{-1}).

spiral arms formed during the coalescence (see Figure 10) do not contain enough mass to alter the waveforms significantly ($M_{tail} \approx 0.05$). Since the total mass of the system is not the same for each run, but increases as the mass ratio is decreased, the peak amplitudes in the waveforms (as well as the peak luminositites) are higher as well for lower q (at a fixed value of Γ). At a fixed value of the initial mass ratio, however, one can observe the effect of using a different adiabatic index clearly. At higher compressibility (i.e. lower Γ), the maximum amplitudes, peak luminosities, the total energy release in gravitational waves and the efficiency of this emission are all higher (see Table 3). The reason for all these trends is the same: the higher the compressibility, the more centrally condensed the star is. For $\Gamma = 5/3$, $\rho_c/\overline{\rho} = 5.99$, while for $\Gamma = 2$, $\rho_c/\overline{\rho} = 3.29$ (ρ_c is the central density of the star and $\overline{\rho}$ is its average density). Thus, it resembles a point mass to a greater degree in the case with $\Gamma = 5/3$ than if $\Gamma = 2$. It is precisely the hydrodynamical effects associated with the star *not* being a point mass that are driving the waveforms and luminosities away from the point–mass result and making them decay. One can also see in Figure 11 that for $\Gamma = 5/3$, the waveform takes longer to begin the decay, and stays close to the point–mass result for a longer time.

5 INFLUENCE OF INITIAL CONDITIONS ON THE DYNAMICAL EVOLUTION OF THE SYSTEM

As for the results we presented in paper III, there are two dynamical runs that have used a spherical star as an initial condition, instead of an irrotational Roche–Riemann ellipsoid. Both have an initial mass ratio $q = 0.31$, one for $\Gamma = 2$ (run C31S) and one for $\Gamma = 5/3$ (run D31S). The initial separation r_i is the same as for runs C31 and D31. The initial orbital angular velocity Ω is that for point–mass binaries, given that the axis ratios are $a_3/a_1 = a_2/a_1 = 1$. The purpose of these runs is to explore the effect of using initial conditions that are far from equilibrium for the calculations of dynamical coalescence. Since we have already perfomed this type of run for a stiff equation of state in paper III, we can also gauge how strong the effects are as a function of the compressibility. We remind the reader that, even if an irrotational Roche–Riemann ellipsoid is a better approximation to the true configuration of the system before coalescence than a spherical star, it is not a *self–consistent* solution, since there are no true equilibrium configurations for such a system. This is simply because the emission of gravitational radiation is always present, and alters the binary separation continuously. A tidal lag angle is always present in the binary, because the bulge on the surface of the neutron star cannot adjust to the changing gravitational potential instantaneously. This angle remains small at large separations, but can become quite large (on the order of 10°, see also Lai, Rasio & Shapiro 1994) just prior to coalescence, when the emission of gravitational waves makes the potential change even faster. This aspect of the coalescence process is greatly influenced by the stiffness of the equation of state.

The strongest effect using a spherical star has on the dynamical coalescence is due to the response of the star to the instantaneous appearance of the gravitational field of the black hole at $t = 0$. A tidal bulge forms, along the line joining the two centres of mass. The deformed star has a greater total energy $W_{self} + U$ (the internal energy decreases, see Figure 14, but the star is less bound by gravity, and the net effect is to increase the energy), which is taken in part from the orbital motion, and so the subsequent decay of the orbit is faster than for runs C31 and D31 (see Figure 13). The

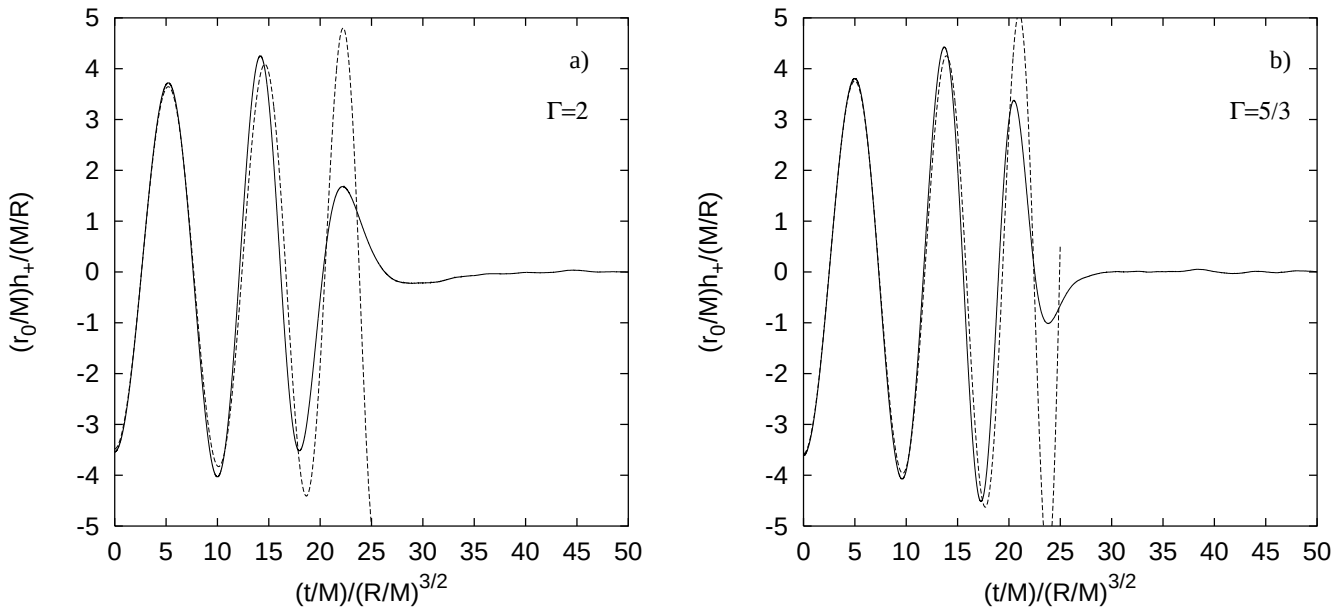

Figure 11. Gravitational radiation waveforms (one polarization is shown) seen at a distance r_0 away from the system along the rotation axis for runs C31 (a), and D31 (b). The dashed lines show the corresponding curves for a point–mass binary with the same initial mass ratio and separation, decaying in the quadrupole approximation. All quantities are given in geometrized units such that $G = c = 1$.

Table 3. Gravitational radiation. All quantities are given in geometrized units such that $G = c = 1$, and $L_0 = c^5/G = 3.64\times10^{59}$ erg s^{-1}.

Run	$(r_0R/M_{\rm NS}^2)h_{max}$	$(r_0R/M_{\rm NS}^2)h_{final}$	$(R/M_{\rm NS})^5(L_{max}/L_0)$	$(R^{7/2}/M_{\rm NS}^{9/2})\Delta E_{GW}$	ϵ
C50	3.00	≤ 0.01	0.58	8.95	$4.15{\cdot}10^{-3}$
C31	4.25	≤ 0.01	1.13	15.38	$5.07{\cdot}10^{-3}$
C31S	4.27	≤ 0.01	1.15	13.79	$4.55{\cdot}10^{-3}$
C20	5.80	≤ 0.01	2.10	24.95	$5.79{\cdot}10^{-3}$
D50	3.19	≤ 0.01	0.87	14.14	$6.57{\cdot}10^{-3}$
D31	4.55	≤ 0.01	1.71	22.29	$7.35{\cdot}10^{-3}$
D31S	4.49	≤ 0.01	1.58	21.86	$7.21{\cdot}10^{-3}$
D20	6.32	≤ 0.01	3.43	38.00	$8.82{\cdot}10^{-3}$

appearance of the tidal bulge also induces radial oscillations in the star, which can be seen in the variations of the total internal energy U, plotted in Figure 14 at early times (compare also with the same curves for a stiff equation of state, in Figure 14b of paper III). The oscillations are always present, but they are somewhat smaller for the runs initiated with ellipsoids.

We shall focus on the results for $\Gamma = 2$ for the following discussion. There are slight variations if $\Gamma = 5/3$ that we will make clear below. As mentioned above, the separation initially decreases faster for run C31S than for run C31. However, the *minimum* separation r_{min} is slighty greater for run C31S (see Figure 13), in contrast to the results shown in paper III. This is again because of the response of the neutron star to mass loss. By expanding and overflowing its Roche lobe further after the initial onset of mass loss, the encounter develops faster, and the stellar core is pushed out to a larger binary separation before approaching the black hole any further. This makes the peak accretion rate lower, the final disc mass higher, and the Kerr parameter of the black hole at $t = t_f$ marginally lower (see Table 2). The gravitational radiation signal is also affected by the initial condition, as can be seen in Table 3. The faster orbital decay gives a higher peak amplitude and luminosity (these quantities depend on the second and third time derivatives of the moment of inertia respectively), but a less energetic and efficient event, because it is more brief.

For $\Gamma = 5/3$, the effect on the disc parameters given in Table 2 is the same as for $\Gamma = 2$. However, there are qualitative differences in the way the gravitational radiation signal is affected. The energetics and efficiency of the events vary in the same way for runs D31 and D31S than for runs C31 and C31S, but the trends are reversed as far as the peak amplitudes and luminosities are concerned. The reason for this is that there are two important factors determining the amplitude (and hence luminosities) of the gravitational radiation waveform: the time derivatives of the moment of inertia, and the mass ratio and separation. Inspection of Figure 13b reveals that the differences between runs D31 and D31S are small indeed. Essentially, the decay is accelerated by using a spherical star, but not nearly fast enough to compensate for the fact that the system attains a greater minimum separation. Thus the peak amplitudes and luminosities are lower for run D31S than for run D31.

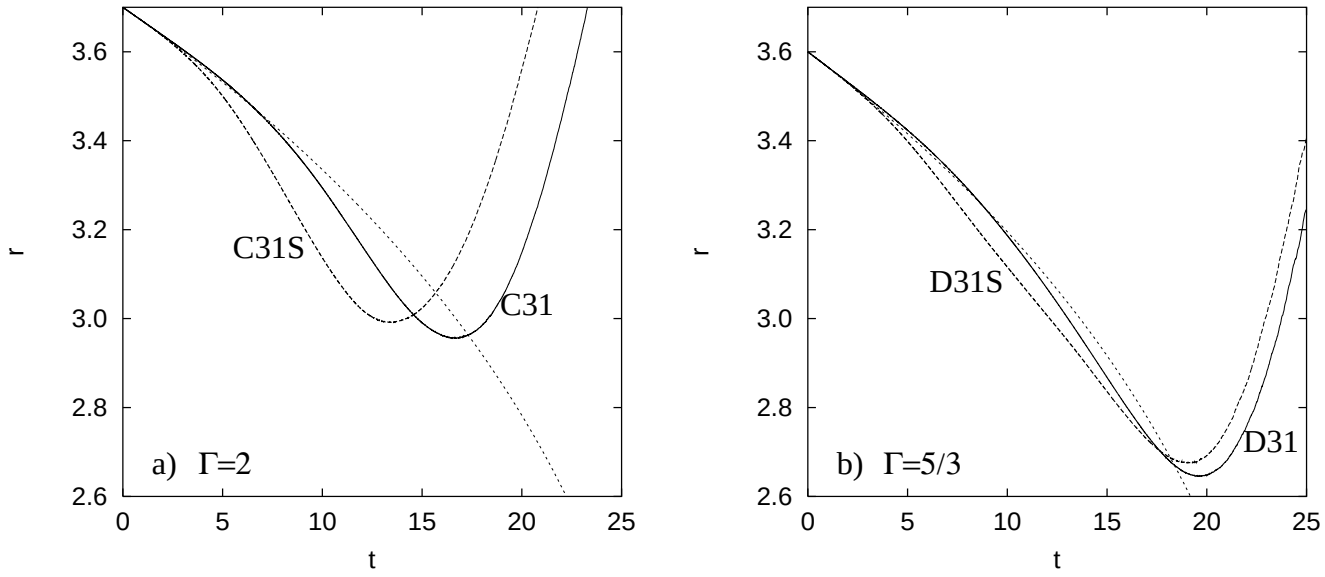

Figure 13. Separation between the black hole and the centre of mass of the neutron star core as a function of time for (a) runs C31 and C31S and (b) runs D31 and D31S. The monotonically decaying lines in each frame are the result for a point–mass binary decaying through gravitational wave emission, in the quadrupole approximation.

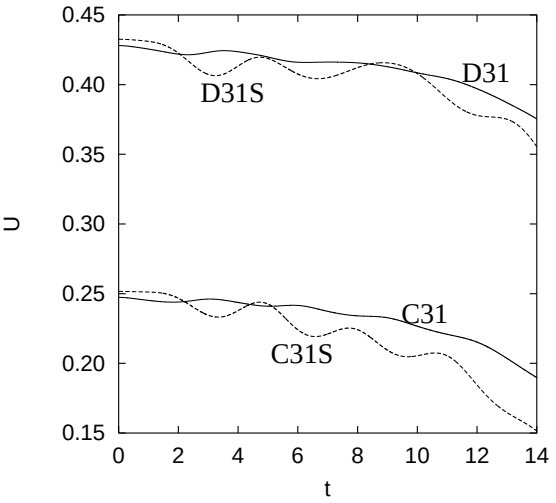

Figure 14. Total internal energy U of the neutron star as a function of time for runs C31, C31S, D31 and D31S.

6 SUMMARY, DISCUSSION AND CONCLUSIONS

We have presented the results of three–dimensional dynamical simulations of the coalescence of a black hole with a neutron star, using Smooth Particle Hydrodynamics. The black hole is modeled as a Newtonian point mass with an absorbing boundary at the Schwarzschild radius $r_{Sch} = 2GM_{BH}/c^2$, and the neutron star is taken as a cold polytrope with adiabatic index $\Gamma = 2$ and $\Gamma = 5/3$. The spatial resolution of the results presented here is the highest we have used to date, with $N \simeq 80,000$ SPH particles modeling the initial neutron star. Dynamical runs with initial mass ratios ranging from $q = M_{NS}/M_{BH} = 0.5$ to $q = 0.2$ were performed. Given that tidal locking is not expected in these systems (Bildsten & Cutler 1992; Kochanek 1992), we have used initial conditions that correspond to irrotational binaries in equilibrium, approximating the neutron star as a compressible tri–axial ellipsoid, following the method of LRSb. The dynamical simulations are begun when the system is on the verge of initiating mass transfer, and followed for approximately 23 ms.

The binary separation decreases as a result of angular momentum losses to gravitational radiation, and the neutron star overflows its Roche lobe within one orbital period after the dynamical simulation is started. Irrespective of the initial mass ratio and of the value of the adiabatic index, this mass transfer episode leads to complete tidal disruption of the star on an orbital time–scale. A massive accretion disc forms around the black hole, containing a few tenths of a solar mass (see Table 2). A single spiral arm appears, from material moving through the outer Lagrange point, farthest from the black hole. Initially, the accretion torus has a complicated structure, with a double ring present (see Figures 2 and 3), as the accretion stream collides with itself and circularizes the orbits of the fluid in the disc. As the simulation progresses, the disc becomes more and more azimuthally symmetric. The peak densities and specific internal energies in the discs at the end of the simulations are on the order of 10^{11}g cm^{-3} and 10^{19} erg g^{-1} respectively (or about 10 MeV nucleon^{-1}). All discs have a low degree of baryon contamination along the rotation axis, directly above and below the black hole (less than $10^{-5}M_{\odot}$ are contained within approximatlely 10° of the rotation axis). The gravitational radiation signal reflects the nature of the encounter,

with the amplitude of the waveforms dropping practically to zero soon after the star is tidally disrupted. Some mass ($M_{ejected} \simeq 10^{-2} M_{\odot}$ at most, see Table 2), found in the outer parts of the tidal tail formed during the initial episode of mass transfer, has enough mechanical energy to be dynamically ejected from the system during coalescence. We find that the amount of ejected mass is sensitive to the value of the adiabatic index, with a sharp drop (by more than two orders of magnitude) ocurring as it decreases below $\Gamma = 2$.

In paper II we showed the results of dynamical calculations of coalescence that used tidally locked binaries with an adiabatic index $\Gamma = 5/3$. Thus the effect of using an irrotational initial condition can be gauged by directly comparing those results with the present ones. The runs shown in paper II also included the effects of gravitational radiation reaction in the quadrupole approximation for point masses, applying it to the whole star, whereas we have now done it by identifying the self–bound core of the neutron star. Qualitatively the outcome of the coalescence is the same for irrotational and tidally locked systems, but there are quantitative differences. These arise because the encounter in the case of a tidally locked binary is more gentle, with the separation decreasing at a slower rate once hydrodynamical effects become important. The details can be seen by comparing the results given for run D in paper II (tidally locked, $\Gamma = 5/3$, initial separation $r_i = 3.60$ and initial mass ratio $q = 0.31$) with those for run D31 shown here. In the former run, the initial peak accretion rate is lower ($\dot{M}_{max} = 0.045$), the final disc mass is higher ($M_{disc} = 0.226$), and the Kerr parameter of the black hole is slightly lower ($a = 0.222$) than for run D31 (where $\dot{M}_{max} = 0.074$, $M_{disc} = 0.141$ and $a = 0.242$), all consistent with a less violent encounter after Roche lobe overflow. The accretion disc itself is not only more massive, but is located at a larger radius, due to the higher value of total angular momentum available in synchronized systems. This can be seen by locating the maximum in the density (which is at $r \simeq 8$ for the tidally locked case, see Figure 10b in paper II, and at $r \simeq 4$ for run D31), and the point at which the distribution of specific angular momentum j flattens, marking the outer edge of the disc (at $r \simeq 13$ for run D in paper II, and at $r \simeq 10$ for run D31). This also makes the maximum densities in the disc greater by at least a factor of five in the irrotational case. The tidal tail is almost nonexistent as a large–scale coherent structure for run D31, but can be seen clearly in the synchronized case (see Figure 11a in paper II). This makes for a lower amount of dynamically ejected mass in the irrotational case (by a factor of 200), and is due to the lower total angular momentum contained in the system, as mentioned above. The exact factor in this case remains somewhat uncertain, since it is sensitive to the implementation of gravitational radiation reaction, which is slightly different in paper II and this work, as mentioned above. In paper II we quoted the dynamically ejected mass as that which had a positive *total* energy, including the internal energy u. Analysis of those simulations reveals that they did contain both type I (cold, dynamically ejected gas) and type II ejected matter (see section 4.3). However, as mentioned above, there was much more dynamically ejected matter than in run D31, and type II matter amounted only to ≈ 5 per cent of the total. Finally, the gravitational radiation signal is affected for the same reasons, with the irrotational case producing a higher maximum amplitude, peak luminosity, and total radiated energy (the differences are of 2, 14 and 7 per cent respectively).

The present results and those given in paper III allow us to observe general trends for all monitored quantities in irrotational systems, as the adiabatic index is lowered from $\Gamma = 3$ to $\Gamma = 5/3$ (see Tables 2 and 3 in paper III and in this work). They can be summarized as follows. As the compressibility increases, the peak accretion rate increases, the disc mass drops (here we exclude the results for $\Gamma = 3$ since that case did not always imply the complete disruption of the neutron star), the black hole has greater spin, the peak amplitude, luminosity and efficiency of gravitational wave emission increase, the disc lifetime decreases, and the minimum separation attained by the binary before tidal disruption is smaller. This last fact implies that the maximum frequency emitted by the system in gravitational waves is higher at lower Γ, and can be seen in Figure 15, where we show the energy spectrum of the gravitational wave signal for different values of Γ at a fixed mass ratio $q = 0.31$. When the binary separation is large compared with the stellar radius, the spectrum is close to that for a point–mass binary, with $dE/df \propto f^{-1/3}$. When the system becomes dynamically unstable, either through tidal effects (for low compressibility) or because of runaway mass transfer (for high compressibility), the power drops abruptly. This occurs at a characteristic frequency f_{dyn}, which increases from $\simeq 700$ Hz to 1 kHz as the adiabatic index decreases from $\Gamma = 3$ to $\Gamma = 5/3$.

Each of these consequences can be traced to the degree of central condensation of the neutron star, to its mass–radius relationship and hence to the way it responds to mass loss upon overflowing its Roche lobe. The magnitude of the changes in the variables mentioned above is not more than a factor of two. The one variable that is greatly affected, especially at low values of Γ, is the total amount of ejected mass (see section 4.3). As mentioned in the introduction, the mass ejected from this type of system might be a source of heavy elements, if the r–process occurs, and could contribute significantly to the observed galactic abundances. Our numerical treatment of the coalescence does not allow us to explore nuclear reactions, but merely estimate how much matter might leave the system. We refer the reader to the work of Rosswog et al. (1999; 2000) and Freiburghaus et al. (1999b) for a detailed thermodynamical and nuclear network calculation, in the case of double neutron star binares. The main point in this respect in our calculations is that (i) ejection is greatly suppressed, and practically eliminated, if the equation of state is very soft and (ii) irrotational systems eject less mass than tidally locked ones, by about one order of magnitude.

The use of accurate equilibrium initial conditions is important in dynamical simulations, since an initial perturbation at the start of the calculation can propagate and affect the evolution of the system. Using spherical neutron stars for one of our chosen mass ratios, $q = 0.31$, we have explored this effect for irrotational binaries, for values of Γ ranging from 3 to 5/3. We find that the qualitative aspect of the coalescence is unaffected, but that quantitative changes occur, all due to the instantaneous appearance of a tidal bulge on the surface of the neutron star as the simulation begins. The effect of this perturbation is largest at low compressibility, since that is when a larger portion of the stellar mass is close to the surface, and tidal effects are more pronounced. As one

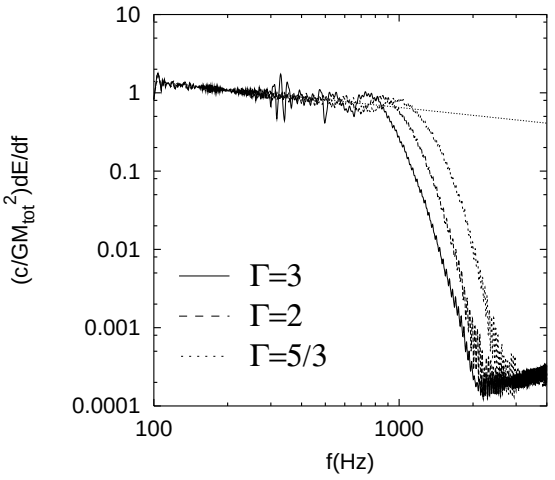

Figure 15. Gravitational waves energy spectrum dE/df for dynamical runs using irrotational binaries with initial mass ratio $q = 0.31$ and $\Gamma = 3$ (solid line, run A31 from paper III), $\Gamma = 2$ (dashed line, run C31) and $\Gamma = 5/3$ (dotted line, run D31). The downward sloping line is the result for a point–mass binary with the same mass ratio, with $dE/df \propto f^{-1/3}$. The increased power at $f \approx 300$ Hz for $\Gamma = 3$ corresponds to the return to low frequencies after the initial mass transfer episode and the survival of the binary (see paper III).

decreases the value of Γ, the differences between runs initiated with spheres (runs A31S and B31S in paper III and runs C31S and D31S in this work) and those that used tri–axial ellipsoids (A31, B31, C31 and D31) become less important.

We have used a polytropic equation of state for our study in order to use the compressibility as a free parameter. Clearly it is an oversimplification as far as thermodynamic details are concerned, but it allows one to explore how the system responds globally to this variable. As we have seen, the emission of gravitational waves and the amount of ejected mass are the two aspects that are most affected by varying Γ. One can make the adiabatic index a function of the density, and in this way try to model the neutron star in a more realistic manner. This approach has been carried out by Rosswog et al. (1999; 2000), although they mainly used the equation of state of Lattimer & Swesty (1991) for their calculations. We have performed tests using this same approximation, and have found that it is the value of Γ at high densities that determines the overall evolution of the system (as Rosswog et al. did), thus fixing for example the qualitative features of the gravitational wave emission and the amount of ejected mass. Realistically, it would appear that the equation of state for neutron star matter is such that the radius is nearly independent of the mass (Prakash & Lattimer 2001), and so adopting a polytropic equation of state would require using $\Gamma = 2$.

In a majority of the dynamical simulations we have performed, we have found that massive accretion discs form, with a few tenths of a solar mass. In all cases when this occurs, the specific angular momentum can be approximated by a power law, with $j \propto r^p$. Regardless of the value of the adiabatic index, the initial mass ratio, or the initial distribution of angular momentum (tidally locked vs. irrotational), we find $p \simeq 0.4 - 0.45$. Thus the discs are sub–Keplerian, and are far from having a constant distribution of specific angular momentum. This is crucial in the context of gamma-ray bursts (see below), because it has been shown that accretion discs around black holes can suffer from a runaway instability that destroys them on a dynamical time–scale (Abramowicz, Calvani & Nobili 1983). Studies over the past two decades have shown that a number of effects can either suppress or enhance it. Among these are (i) the spin of the black hole, (ii) the rotation law in the disc, specified as $j \propto r^p$, (iii) the effects of general relativity and (iv) the self–gravity of the disc. Factors (i–high spin) and (ii–increasing the value of p) tend to suppress the instability (Wilson 1984; Daigne & Mochkovitch 1997; Abramowicz, Karas & Lanza 1998; Masuda, Nishida & Eriguchi 1998; Lu et al. 2000), while (iii) and (iv) tend to enhance it (Nishida et al. 1996; Nishida & Eriguchi 1996; Masuda, Nishida & Eriguchi 1998). We note here that all of these studies assume a softer equation of state than the ones we have used (either using a polytrope with $\Gamma = 4/3$ or a realistic equation of state for neutron tori). Since our simulations show that the Kerr parameter of the black hole is significant, and that the power–law index of the distribution of specific angular momentum is high, it would appear that these discs would not suffer from the aforementioned instability, and would thus evolve due to angular momentum transport on the much longer viscous (rather than dynamical) time–scale. However, our simulations are purely Newtonian, and thus it is impossible to include the de–stabilizing effects of general relativity. The mass of the discs we find is apparently not too high (Masuda & Eriguchi 1997), regarding the criterion for self–gravity (the mass ratio $q_{disc} = M_{disc}/M_{BH}$ between the disc and the black hole at the end of the calculations for irrotational binaries ranges between 0.02, for run D20, and 0.09, for run B50 in paper III).

The accretion discs always have a baryon–free region along the rotation axis, above and below the black hole. This region is clear of matter to a degree (less than $10^{-5} M_\odot$ within approximately 10°) that would not hinder the production of a relativistic fireball (Mészáros & Rees 1992; Mészáros & Rees 1993), thus powering a cosmological gamma ray burst. The binding energy of the tori is $\simeq 10^{52}$ erg (see e.g. Figure 6), and the Kerr parameter of the black hole is $a \simeq 0.3$ at the end of the calculations, so the energy for the burst could come either from neutrino emission from the disc or from the spin of the black hole via the Blandford & Znajek (1977) mechanism if the magnetic field in the torus is strong enough and threads the black hole. The maximum extractable energy in this latter case would be $\simeq \epsilon_{BZ} 10^{53}$ erg, where ϵ_{BZ} is the MHD efficiency factor. In either case, one would expect the disc to survive for a time–scale comparable to the duration of the burst, i.e. on the order of seconds. This is why the previously mentioned result concerning the power law distribution of angular momentum and the accompanying dynamical stability of the disc is so important. The short time–scales and rapid variability involved in a small (≈ 100 km) accretion disc around a black hole make these systems attractive candidates for the central engines of short gamma ray bursts, as we found in our preliminary studies (Kluźniak & Lee 1998), and have now confirmed in the present series of papers for a wide vari-

ety of initial conditions, varying the stiffness of the equation of state, the initial mass ratio in the binary and the distribution of angular momentum in the system.

We note that the mounting observational evidence in favor of massive stars being GRB progenitors (Galama & Wijers 2001) does not exclude compact mergers as sources, simply because all observed afterglows, from which the inferences about the environment where the bursts occur come, correspond to long bursts. If compact mergers do in fact produce GRBs, spectacular confirmation about the nature of the source could be obtained through the detection of a coincident gravitational wave signal, even if the final coalescence waveform is outside the frequency band of detectors such as LIGO. One could observe the final minutes of the inspiral phase as the orbital frequency increases, leaves the LIGO band, and then search for a coincident GRB.

ACKNOWLEDGMENTS

This work has benefited greatly from conversations with Włodzimierz Kluźniak, Frederic Rasio, Maximilian Ruffert and Lars Bildsten. I thank the referee for a thorough reading of the manuscript and a prompt report, and for pointing out the error in the calculation of the Kerr parameter of the black hole. Support for this work was provided by CONACyT (27987E) and DGAPA–UNAM (IN-119998).

REFERENCES

Abramovici M. et al. 1992, Science, 256, 325
Abramovicz M. A., Calvani M., Nobili L. 1983, Nat., 302, 597
Abramovicz M. A., Karas V., Lanza A. 1998, A& A, 331, 1143
Ayal S., Piran T., Oechslin R., Davies M. B., Rosswog S. 2001, ApJ, 550, 846
Balsara D. 1995, J. Comp. Phys., 121, 357
Baumgarte T. W., Cook G. B., Scheel M. A., Shapiro S. L., Teukolsky S. A. 1997, Phys. Rev. Lett., 79, 1182
Belczyński K., Bulik T. 1999, A&A, 346, 91
Bethe H. A., Brown G. E. 1998, ApJ, 506, 780
Bildsten L., Cutler C. 1992, ApJ, 400, 175
Blanchet L., Damour T., Iyer B. R., Will C. M., Wiseman A. G. 1995, Phys. Rev. Lett., 74, 3515
Blandford R. D., Znajek R. L. 1977, MNRAS, 179, 433
Bradaschia C. et al. 1990, Nucl. Instrum. Methods Phys. Res., Sect. A, 289, 518
Chandrasekhar S. 1969, Ellipsoidal figures of equilibrium, (New Haven: Yale Univ. Press)
Cutler C. et al. 1993, Phys. Rev. Lett., 70, 2984
Daigne F., Mochkovitch R. 1997, MNRAS, 285, L15
Davies M. B., Benz W., Piran T., Thielemann F.–K. 1994, ApJ, 431, 742
Djorgovski S. G., Kulkarni S. R., Bloom J. S., Goodrich R., Frail D. A., Piro L., Palazzi E. 1998, ApJ, 508, L17
Eichler D., Livio M., Piran T., Schramm D. N. 1989, Nat., 340, 126
Faber J. A., Rasio F. A. 2000, Phys. Rev. D, 62, 064012
Faber J. A., Rasio F. A., Manor J. B. 2001, Phys. Rev. D, 63, 044012
Finn L.S. 1989 in Evans C. R., Finn L. S., Hobill D. W., eds, Frontiers of Numerical Relativity, Cambridge Univ. Press. Cambridge, p.126
Fishman G. J., Meegan C. A. 1995, ARA&A, 33, 415
Frail D. A. et al. 2001, Nat., submitted, astro-ph/0102282
Freiburghaus C., Rembges J.–F., Rauscher T., Kolbe E., Thielemann F.–K. 1999a, ApJ, 516, 381
Freiburghaus C., Rosswog S., Thielemann F.–K. 1999b, ApJ, 525, L121
Fryer C. L., Woosley W. E., Hartmann D. H., 1999a, ApJ, 526, 152
Fryer C. L., Woosley W. E., Herant M., Davies M. B. 1999b, ApJ, 520, 650
Galama T. J., Wijers R. A. M. J. 2001, ApJ, 549, L209
Goodman J. 1986, ApJ, 308, L46
Goodman J., Dar A., Nussinov S. 1987, ApJ, 314, L7
Gourgoulhon E., Grandclement P., Taniguchi K., Marck J.–A., Bonazzola S. 2001, Phys. Rev. D, 63, 064029
Harrison F. A. et al. 1999, ApJ, 523, L121
Hulse R. A., Taylor J. H. 1975, ApJ, 195, L51
Janka H.–Th., Eberl T., Ruffert M., Fryer C. L. 1999, ApJ, 527, L39
Jaroszyński M. 1993, Acta Astron., 43, 183
Jaroszyński M. 1996, A&A, 305, 839
Kalogera V., Narayan R., Spergel D. N., Taylor J. H. 2001, ApJ, 556, 340
Kalogera V., Belcyński K. 2001, in Centrella J., ed., AIP Proc. 575, Astrophysical sources for ground–based gravitational wave detectors, AIP, New York, p. 107, astro-ph/0101047
Kidder L. E., Will C. M., Wiseman A. G., 1992, Class. Quantum Grav., 9, L125
Kluźniak W., Lee W. H. 1998, ApJ, 454, L53
Kluźniak W., Ruderman M. 1998, ApJ, 505, L113
Kochanek C. 1992, ApJ, 398, 234
Kouveliotou C., Koshut T., Briggs M. S., Pendleton G. N., Meegan C. A., Fishman G. J., Lestrade J. P. 1995, in Kouveliotou C., Briggs M. F., Fishman G. J., eds., AIP Proc. 384, Gamma Ray Bursts, AIP, New York, p. 42
Kulkarni S. R. et al. 1998, Nat., 393, 35
Kulkarni S. R. et al. 1999, Nat., 398, 389
Lai D., Rasio F. A., Shapiro S. L. 1993a, ApJ, 406, L63 (LRSa)
Lai D., Rasio F. A., Shapiro S. L. 1993b, ApJS, 88, 205 (LRSb)
Lai D., Rasio F. A., Shapiro S. L. 1994, ApJ, 437, 742
Landau L.D., Lifshitz E.M. 1975, The Classical Theory of Fields, Heinemann, Oxford
Lattimer J. M., Schramm D. N. 1974, ApJ, 192, L145
Lattimer J. M., Schramm D. N. 1976, ApJ, 210, 549
Lattimer J. M., Swesty D. 1991, Nuc. Phys. A, 535, 331
Lee H. K., Wijers R. A. M. J., Brown G. E. 2000, Phys. Rep. 325, 83
Lee W. H. 1998, PhD Thesis, University of Wisconsin
Lee W. H., Kluźniak W. 1995, Acta Astron., 45, 705
Lee W. H., Kluźniak W. 1997, in Meegan C., Preece R., Koshut P. eds., AIP Proc. 428, Gamma Ray Bursts, AIP, New York, p. 798
Lee W. H., Kluźniak W. 1999a, ApJ, 526, 178 (paper I)
Lee W. H., Kluźniak W. 1999b, MNRAS, 308, 780 (paper II)
Lee W. H. 2000, MNRAS, 318, 606 (paper III)
Lipunov V. M., Postnov K. A., Prokhorov M. E., 1997, New Ast., v.2, 43
Lombardi J. C., Rasio F. A., Shapiro S. L., 1997, Phys. Rev. D, 56, 3416
Lu Y., Cheng K. S., Yang L. T., Zhang L. 2000, MNRAS, 314, 453
MacFadyen A., Woosley S. E. 1999, ApJ, 524, 262
Masuda N., Eriguchi Y. 1997, ApJ, 489, 804
Masuda N., Nishida S., Eriguchi Y. 1998, MNRAS, 297, 1139
Meegan C. A., Fishman G.J., Wilson R. B., Horack J. M., Brock M. N., Paciesas W. S., Pendleton G. N., Kouveliotou, C. 1992, Nat., 355, 143
Metzger M. R., Djorgovski S. G., Kulkarni S. R., Steidel C. C., Adelberger K. L., Frail D. A., Costa E., Frontera F. 1997, Nat., 387, 878

Mészáros P., Rees M. J. 1992, MNRAS, 257, 29P
Mészáros P., Rees M. J. 1993, ApJ, 405, 278
Mészáros P., Rees M. J. 1997a, ApJ, 476, 232
Mészáros P., Rees M. J. 1997b, ApJ, 482, L29
Mészáros P., Rees M. J., Wijers R. A. M. J. 1999, New Ast., 4, 303
Meyer B. S., Brown J. S. 1997, ApJS, 112, 199
Mochkovitch R., Hernanz M., Isern J., Martin X. 1993, Nat., 361, 236
Mochkovitch R., Hernanz M., Isern J., Loiseau S. 1995, A& A,293, 803
Monaghan J. J. 1992, ARA&A, 30, 543
Nakamura T., Oohara K. 1989, Prog. Theor. Phys., 82, 1066
Nakamura T., Oohara K. 1991, Prog. Theor. Phys., 86, 73
Narayan R., Paczyński B., Piran T., 1992, ApJ, 395, L83
Narayan R., Piran T., Shemi A. 1991, ApJ, 379, L17
Nishida S., Lanza A., Eriguchi Y., Abramowicz M. A. 1996, MNRAS, 278, L41
Nishida S., Eriguchi Y. 1996, ApJ, 461, 320
Oohara K., Nakamura T. 1989, Prog. Theor. Phys., 82, 535
Oohara K., Nakamura T. 1990, Prog. Theor. Phys., 83, 906
Oohara K., Nakamura T. 1992, Prog. Theor. Phys., 88, 307
Oohara K., Nakamura T. 1999, Prog. Theor. Phys. Supp., 136, 270
Paczyński B. 1986, ApJ, 308, L43
Paczyński B. 1991, Acta Astron., 41, 257
Popham R., Woosley S. E, Fryer C. 1999, ApJ, 518, 356
Portegies Zwart S. F., Yungelson L. F. 1998, A&A, 372, 173
Prakash M., Lattimer J. M. 2001, ApJ, 550, 426
Rasio F. A., Shapiro S. L. 1992, ApJ, 401, 226 (RS92)
Rasio F. A., Shapiro S. L. 1994, ApJ, 432, 242 (RS94)
Rasio F. A., Shapiro S. L. 1995, ApJ, 438, 887 (RS95)
Rees M. J., Mészáros P. 1992, MNRAS, 258, 41P
Rosswog S., Liebendörfer M., Thielemann F.–K., Davies M. B., Benz W., Piran T. 1999, A&A, 341, 499
Rosswog S., Davies M.B., Thielemann F.–K., Piran T. 2000, A&A, 360, 171
Ruderman M., Tao L., Kluźniak W. 2000, ApJ, 542, 243
Ruffert M., Janka H.–Th., Schäfer G. 1996, A&A, 311, 532
Ruffert M., Janka H.–Th., Takahashi K., Schäfer G. 1997, A&A, 319, 122
Ruffert M., Janka H.–Th. 1999, A&A, 344, 573
Salmonson J. D., Wilson J. R., Mathews G. J. 2001, ApJ, 553, 471
Shibata M. 1999, Phys. Rev. D, 60, 104052
Shibata M., Uryū K. 2000, Phys. Rev. D, 61, 064001
Spruit H. 1999, A&A, 341, L1
Stairs I. H., Arzoumanian Z., Camilo F., Lyne A. G., Nice D. J., Taylor J. H., Thorsett S. E., Wolszczan A., 1998, ApJ, 505, 352
Stanek K. Z., Garnavich P. M., Kaluzny J., Pych W., Thompson I. 1999, ApJ, 522, L39
Symbalisty E. M. D., Schramm D. N. 1982, Astrophyscial Letters, 22, 143
Taylor J. H., Wolszczan A., Damour T., Weisberg J.M. 1992, Nat., 355, 132
Thompson C. 1994, MNRAS, 270, 480
Tutukov A. V., Yungelson L. R. 1993, MNRAS, 260, 675
Uryū K., Eriguchi Y. 1999, MNRAS, 303, 329
Uryū K., Eriguchi Y. 2000, Phys. Rev. D, 2000, 61, 124023
Usov V. V. 1992, Nat., 357, 472
Usui F., Uryū K., Eriguchi Y. 2000, Phys. Rev. D, 2000, 61, 024039
van Paradijs J., Kouveliotou C., Wijers R. A. M. J. 2000, ARA&A, 38, 379
Wheeler J. A. 1971, Pontificae Acad. Sci. Scripta Varia, 35, 539
Wilson D. B. 1984, Nat., 312, 620
Wilson J. R., Mathews G. J., Marronetti P., 1996, Phys. Rev. D, 54, 1317
Witt H. J., Jaroszyński M., Haensel P., Paczyński B., Wambsganss J. 1994, ApJ, 422, 219
Wolszczan A. 1991, Nat., 350, 688
Woosley S. E. 1993, ApJ, 405, 273
Zhang W., Fryer C. L. 2001, ApJ, 550, 357
Zhuge X., Centrella J. M., McMillan S. L. W., 1994, Phys. Rev. D, 50, 6247
Zhuge X., Centrella J. M., McMillan S. L. W., 1996, Phys. Rev. D, 54, 7261.

APPENDIX A: COMPUTATION OF THE KERR PARAMETER OF THE BLACK HOLE

The Kerr parameter a of the black hole was incorrectly calculated for the results presented in papers II and III. In this appendix we show explicitly the correct derivation of $J_{\rm BH}^{spin}$, and the corrected values for all the runs performed in papers II and III.

When a gas (SPH) particle crosses the accretion boundary of the black hole, set at the Schwarzschild radius $r_{Sch} = 2GM_{\rm BH}/c^2$, we update the mass and velocity of the black hole so as to ensure conservation of mass and total linear momentum, i.e.

$$M'_{\rm BH} = M_{\rm BH} + m_i, \tag{A1}$$

and

$$M'_{\rm BH}\vec{v}'_{\rm BH} = M_{\rm BH}\vec{v}_{\rm BH} + m_i\vec{v}_i, \tag{A2}$$

where primed quantities refer to values after the particle has been accreted and removed from the simulation.

The conservation of total angular momentum reads:

$$\vec{r}_i \times m_i\vec{v}_i + \vec{r}_{\rm BH} \times M_{\rm BH}\vec{v}_{\rm BH} = \vec{r}'_{\rm BH} \times M'_{\rm BH}\vec{v}'_{\rm BH} + \vec{J}_{\rm BH}^{spin}, \tag{A3}$$

where $J_{\rm BH}^{spin}$ is the spin angular momentum gained by the black hole because of the accretion. A fraction of the particle's angular momentum contributes to the orbital angular momentum of the black hole, and the rest to its spin. In practice, we found that the latter term dominates, and that our error was due mainly to not taking into account the angular momentum lost to gravitational waves (which is most important in the early stages of the simulation, before the neutron star has been disrupted). Table A1 shows the correct values for the Kerr parameter of the black hole for the runs shown in paper II (A through E) and for those presented in paper III (A50, A31, A31S, A20, B50, B31S, B31 and B20).

Table A1. Kerr parameter of the black hole at the end of the dynamical simulations for the runs presented originally in papers II and III

Run	Γ	q	$J_{\rm BH}c/GM_{\rm BH}^2$	Reference
A	5/3	1.00	0.448	paper II
B	5/3	0.80	0.409	paper II
C	5/3	0.31	0.232	paper II
D	5/3	0.31	0.222	paper II
E	5/3	0.10	0.097	paper II
A50	3.0	0.50	0.339	paper III
A31	3.0	0.31	0.226	paper III
A31S	3.0	0.31	0.238	paper III
A20	3.0	0.20	0.156	paper III
B50	2.5	0.50	0.339	paper III
B31	2.5	0.31	0.244	paper III
B31S	2.5	0.31	0.247	paper III
B20	2.5	0.20	0.167	paper III